UNIVERSIDADE DA BEIRA INTERIOR
Engenharia

Combustion analysis on a CFM56-3 engine

Kevin Azevedo das Neves

Dissertação para obtenção do Grau de Mestre em
Engenharia Aeronáutica
(Ciclo de estudos integrado)

Orientador: Prof. Doutor Francisco Miguel Ribeiro Proença Brojo

Covilhã, Fevereiro de 2018

Dedication

To my beloved parents, Patrocínia and Fernando Neves, who have always been an inspiration and to whom I owe everything.

To my brother and sister, Lucas and Melisa, who I unconditionally love and to whom I wish the brightest future.

A smooth sea never made a skilled sailor.

Franklin D. Roosevelt

Acknowledments

I would like to thank my family who have always supported me and gave me freedom to persue my dreams. All the goals I have accomplished so far and the person I stand today are due to your inconditional care.

A big thank you to my supervisor, Professor Francisco Brojo, who have always kept me in the right path during this challenging time. I will always be grateful for your guidance and constant support. I can not describe how grateful I am for the availability and promptitude when I needed help.

I am deeply grateful to my Executive Board of AIESEC in Covilhã UBI, who I can not be more honored to have had the opportunity to lead during the last year. Patrícia, Alexandre and Maria, you embraced this huge challenge with me and I can not thank you enough for helping me evolving our committee to a whole new level. With you, I learned so much and I spent some of the greatest moments of this year.

For all AAUBI 2017 team, I want to thank you for all the opportunities I had with you and for each memorable moment I will never forget. Thank you for being able to really take an active role in the improvement of our students community.

I am profoundly grateful to my dearest friend Robert Gonçalves, who have raised this passion for aeronautics in me, and who was always a great companion to talk to during the last five years.

Last but not least, I would like to thank all my friends from Pombal, Belo Horizonte and Covilhã, specially to Rafael, who made my academic experience unique.

Resumo

Quanto mais eficiente um motor é, menos combustível é necessário para ir de um ponto A para um ponto B e menos gases de efeito estufa são produzidos. Apesar de serem uma fonte de dióxido de carbono significante, os motores de turbina de gás lideram os sistemas de propulsão aeronáutica e provavelmente assim vão continuar nas próximas décadas. Portanto, uma das formas mais rápidas de procurar ser sustentável nos céus é melhorando a sua *performance*. Todavia, estes motores representam um dos mais complexos problemas de engenharia, uma vez que dependem de centenas de diferentes parâmetros que ao variarem podem levar a que surja uma configuração melhor. No entanto, disponibilizamos de computadores e *softwares* capazes de testar diferentes conceitos. Este trabalho consistiu em uma análise numérica da combustão de Jet-A no combustor anular do CFM56-3, através de dois modelos de turbulência diferentes. A geometria utilizada foi ¼ do motor construído pelo Jonas Oliveira, ao realizer um scan 3D a um combustor real. Esta geometria foi importada para um software de CFD, CONVERGE Studio, onde todos os parâmetros dos ensaios foram configurados. A simulação em sim foi realizada no *software* principal CONVERGE, instalado num computador de alto desempenho. O objetivo final deste estudo passou pela comparação do comportamento de cada modelo de turbulência, enquanto estudamos a performance de um dos mais populares motores turbofan. Os modelos de turbulência escolhidos foram o *standard* k-ε e o *standard* k-ω, para além de ter sido selecionado um conjunto de modelos para simular a injeção de combustível através de vaporização, de modo a prever melhor o comportamento do escoamento dentro do combustor. De forma a comparar estes modelos, seis parâmetros principais foram analisados: a enregia cinética turbulenta (k); a taxa de dissipação da energia cinética turbulenta (ε); a dissipação da energia cinética turbulenta específica (ω); o comprimento característico dos turbilhões (l); a velocidade de fricção (u^*); e a distância adimensional à parede (y^+). Ambos os modelos mostraram um comportamento semelhante ao longo do tempo para todos os parâmetros. Todos os resultados encontram-se na mesma ordem de grandeza, apesar apresentarem uma diferença considerável no seu valor absoluto. Os mesmos foram considerados aceitáveis, após uma comparação quantitativa com parâmetros à saída do combustor e uma comparação qualitativa de um perfil de temperaturas e de um perfil de energia cinética turbulenta com dois estudos de configurações similares. Por fim, nenhum modelo foi classificado melhor que o outro, devido à complexidade envolvida num estudo deste tipo, mas apenas considerados diferentes.

Palavras-chave

Combustão; Turbulência; Modelo; CFM56-3; Jet-A; CFD; CONVERGE.

Abstract

The more fuel efficient an engine is, the less fuel is needed to get from point A to point B and the less Greenhouse gases will be produced. In spite of being a major source of carbon dioxide, gas turbine engines lead the aircraft propulsion systems globally and will probably continue for the next decades. Thus, one of the most immediate ways to go green on the skies is by advancing their performance. Nontheless, GTE's are one of the most complex engineering problems, as they rely on hundreds of parameters that can be tweaked and result in a better configuration. However, we have computers and softwares that allow us to test engine concepts. This study consisted in a numerical analyses of the combustion of Jet-A in the annular combustor of the CFM56-3 engine, through two different turbulence models. The geometry used was ¼ of the engine constructed by Jonas Oliveira by performing a 3D scan on a real size combustor. This geometry was imported and prepared in a CFD software, CONVERGE Studio, where the case setup was configured. The simulation itself was run on the main software CONVERGE installed on a multi-core high performance machine. The final goal of this study was to compare the behavior of each turbulence model when studying the performance of annular combustors similar to the most popular turbofan engine's. The turbulence models chosen were the standard k-ε and the standard k-ω and also a set of models were defined to simulate the injection of fuel through a parcel spray and, therefore, better predict the flow inside the combustor. To compare the simulation results, six main parameters were analysed: Turbulent Kinematic Energy (k); Turbulence Dissipation Rate (ε); Specific Turbulence Dissipation Rate (ω); Turbulent Length Scale (l); Friction Velocity (u^*); and the dimensionless wall distance (y^+). Both models demonstrated a similar behavior in all the parameters, along the runtime. The results were all within the same order of magnitude, although the absolute values have shown a considerable difference. The simulation outputs were considered acceptable after comparing quantitatively the exhaust parameters, and qualitatively a temperature and TKE contour with two previous works with similar setup conditions. Any turbulence model was judged better than the other, due to the complexity involved in such a study, but only considered different.

Keywords

Combustion; Turbulence; Model; CFM56-3; Jet-A; CFD; CONVERGE.

Contents

List of Figures

List of Tables

List of Acronyms

AFR	Air to Fuel Ratio
AMR	Adaptive mesh Refinment
ASCII	American Standard Code for Information Interchange
ASM	Algebraic Stress Model
CEQ	Chemical EQuilibrium
CFD	Computational Fluid Dynamics
CTC	Characteristic Time Combustion
DNS	Direct Numerical Simulation
ECFM	Extended Coherent Flame Model
FGM	Flamelet Generated Manifold
GHG	Green House Gases
GTE	Gas Turbine Engine
HPC	High Pressure Compressor
HPT	High Pressure Turbine
ICAO	International Civil Aviation Organization
LES	Large Eddy Simulation
PZ	Primary Zone
RAM	Random Access Memory
RANS	Reynolds-Averaged Navier-Stokes
RIF	Representative Interactive Flamelet
RNG	Re-Normalisation Group
RSM	Reynolds Stress Model
SAS	Scale-Adaptive Simulation
SGS	Sub Grid Scale
SST	Shear Stress Transport
SZ	Secondary Zone
TAP	Transportes Aéreos de Portugal
TKE	Turbulent Kinetic Energy
UBI	Universidade da Beira Interior

Nomenclature

A	Area	$[m^2]$
B	Wall roughness constant	$[-]$
$C_{\varepsilon 1}$	k-ε model constant	$[-]$
$C_{\varepsilon 2}$	k-ε model constant	$[-]$
C_{μ}	k-ε model constant	$[-]$
$C_{\varepsilon 1}$	k-ε model constant	$[-]$
C_S	Smagorinsky constant	$[-]$
f_{β}	k-ω model constant	$[-]$
f_{β^*}	k-ω model constant	$[-]$
h	Absolute enthalpy	$[J/kg]$
h_f	Enthalpy of formation	$[J/kg]$
Δh_r	Enthalpy of combustion	$[J/kg]$
m	Mass	$[kg]$
$\dot{m}$	Mass flow rate	$[kg/s]$
k	Turbulent kinematic energy	$[m^2/s^2]$
l	Lenghtscale	$[m]$
l_0	Lenghtscale of the largest eddies	$[m]$
l_{EI}	Demarcation lengthscale between the energy-containing and smaller eddies	$[m]$
p	Pressure	$[Pa]$
P	Time-averaged pressure	$[Pa]$
q	Heat	$[J]$
Re	Reynolds number	$[-]$
s	Strain-rate tensor	$[N/m^2.s]$
S	Mean strain-rate tensor	$[N/m^2.s]$
t	Time	$[s]$
T	Temperature	[K]
u	Velocity	$[m/s]$
u^+	Dimensionless Velocity	$[-]$
u_*	Friction velocity	$[m/s]$
u_{η}	Kolmogorov velocity scale	$[m/s]$
U	Time-averaged velocity	$[m/s]$
y^+	Dimensionless Wall distance	$[-]$

Greek letters

α	k-ω model constant	$[-]$
β	k-ω model constant	$[-]$
β^*	k-ω model constant	$[-]$
β_o	k-ω model constant	$[-]$
β_o^*	k-ω model constant	$[-]$
δ	Boundary-layer thickness	$[m]$
ε	Turbulent dissipation rate	$[m^2/s^3]$
η	Kolmogorov lengthscale	$[m]$

κ	Karman constant	$[-]$
μ	Absolute viscosity	$[Pa.s]$
μ_t	Molecular eddy viscosity	$[Pa.s]$
ν	Kinematic viscosity	$[m^2/s]$
ν_T	Kinematic eddy viscosity	$[m^2/s]$
ρ	Density	$[kg/m^3]$
σ	k-ω model constant	$[-]$
σ^*	k-ω model constant	$[-]$
σ_k	k-ε model constant	$[-]$
σ_ε	k-ε model constant	$[-]$
τ_η	Kolmogorov timescale	$[s]$
τ_{ij}	Stress tensor	$[N/m^2]$
ω	Specific turbulent dissipation rate	$[1/s]$

Upper-case Greek

Δ	Filter width	$[m]$

Subscripts

a	Air
ad	Adiabatic
f	Fuel
prod	Products
reac	Reactants
ref	Reference
t	Turbulent
i, j	Coordinate directions

Chapter 1

Introduction

1.1 Motivation

The most popular and commode way to go from point A to point B, if we are speaking about long distances, is by airplane. Today, most of the aircrafts use combustion to power its engines. Combustion has been present on aviation almost since the beginning of its history. It was in 1903, after four years of experimental work with gliders, that the Wright brothers flew for the first time with their heavier-than-air craft, which was powered by a $12\,hp$ $(8.9\,kW)$ engine [1]. It was a four-cylinder, water-cooled, internal-combustion and first gasoline engine to fly designed by themselves. The aircraft propulsion has come a long way since then, and the current state-of-the-art CFM56 turbofan engine family is the proof of the disruptive evolution. And not only it has the potential to go further, but also need to go further, once gas engines will be in our airplanes for next decades. The World Energy Council states on its 2016 Resources Report that oil remained the world's leading fuel, accounting for 32.9% of global energy consumption; roughly 63% of oil consumption is from the transport sector. Oil substitution is not yet imminent and is not expected to reach more than 5% for the next five years [2]. Hence, one of the most immediate ways to go green on the skies is by advancing gas turbine engines. Carbon dioxide is one of the major sources of Greenhouse Gases. Besides, CO_2, along with water vapor is also the product of a complete combustion. So, the more fuel efficient our engine is, the less fuel is needed to get from point A to point B and the less carbon dioxide will be produced.

We have made significant strides in fuel efficiency, the average fuel burn of a new aircraft fell by about 45% from 1968 to 2014 [3] and we will keep improving in order to keep up with regulations and ICAO's technology goals. We have been able to reduce emissions and improve fuel efficiency by innovating. However, before we discuss how we can innovate in gas turbine engines, we need to understand how such engines work. A jet engine keeps an aircraft moving forward using a very simple principle. The same that makes an air filled balloon move: Newton's 3rd law of motion. Just like the reaction force produced by the air moves the balloon, the reaction force produced by the high speed jet at the tail of the engine makes it move forward. Thus, the working of a jet engine is all about a high speed jet at the exit. The higher the speed of the jet, the greater the thrust force. Such high-speed exhaust is achieved by a combination of techniques. By heating the incoming air to a high temperature, it will expand tremendously and will create the high velocity jet. For this purpose, a combustion chamber is used where an atomized form of the fuel is burnt inside. Effective combustion requires air to be at moderately high temperature and pressure. To bring the air to this condition, a set of compressor stages is used. The rotating blades of the compressor add energy to the fluid and its temperature and pressure rise to a level suitable to sustain combustion. A compressor receives the energy for the rotation from a turbine, which is placed right after the combustion chamber. The compressor and turbine are attached to same shaft. The high-energy fluid that leaves the chamber makes the turbine blades turn. As the turbine absorbs energy from the fluid, its pressure drops. Also, the engine case becomes narrower towards the outlet, which results in even greater jet velocity. In short, the synchronized of the compressor, combustion chamber and turbine makes the aircraft move forward. A revolutionary improvement was made by fitting a large fan with a low pressure spool and a low pressure turbine, giving rise to the what we call today turbofan engines. Almost every commercial aircraft runs on them nowadays, being the CFM56 family, a popular example. In these engines, some of the incoming air passes through the fan and continues on into the core compressor and then the burner, where it is mixed with fuel and combustion occurs. The hot exhaust passes through the core and fan turbines and then out the nozzle, as in a basic turbojet. The rest of the incoming air passes through the fan and bypasses, or goes around the engine, just like the air through a propeller. The ratio of the air that goes around the engine to the air that goes through the core is called the bypass ratio. In an engine with a bypass ratio of 5:1, for every 6 units of air drawn into the engine, 5 will bypass the engine core and 1 will go through it. In a turbofan engine, the majority of the thrust force comes from the fans reaction force. The fan greatly improves airflow in the system by absorbing more air, improving the thrust. This means, high thrust creation with an expense of slightly more fuel is the reason why turbofan engines are highly fuel economical. This better fuel economy, together with quieter exhaust, are responsible for the domination of the aircraft propulsion systems by these engines. Gas turbine engines are one of the most complex engineering problems out there. It relies on turbulent flow, fuel injection, fuel properties, fuel chemistry, fuel spray, combustion chamber, among many others. There are literally hundreds of parameters that can be tweaked in an engine to come up with an optimal configuration. Although, the greenest engine, which is our goal, is this optimal combination and we need to find it.

Finding that is not easy, once we can not build and test engines for all the combination of parameters. However, we have computers and softwares that allow us to test engine concepts before we build them. And we have optimization software that allow us to run a reduced set of designs in order to find an optimum. These tools, along with experiments have helped to meet emissions and fuel economy mandates throughout regulation history. The engines keep improving, partly because airlines want to fill up their tanks less often, but also because the regulations are forcing engine makers to find solutions in order to keep selling aircrafts. The computer softwares we have to simulate these engines before building them are really advanced, but far from perfect under a lot of conditions and it takes a long time to run. Computer methods and speeds both need to improve significantly to get us better answers quicker, but it is worth the effort as it is an important key to allow us to go greener.

1.2 Main Goal

The present work consists in a numerical analyses of the combustion of Jet-A in the annular combustor of the CFM56-3 engine, through two different turbulence models. The geometry used was ¼ of the engine constructed by Jonas Oliveira [4] by performing a 3D scan on a real size combustor, gently provided by TAP, in which all the measurements were extracted to conduct a Computer Assisted Design with the commercial software CATIA V5. This geometry was imported to a Computer Fluid Dynamics software, CONVERGE Studio, where the case setup was configured. Then, the simulation was run on the main software CONVERGE installed on a multi-Core High Performance computer. After the simulation, the results were visualized and post-processed in CONVERGE Studio.

The turbulence models chosen were the *Standard* k-ε and the *Standard* k-ω. As we can not claim that any model is better than another, once it depends on the case, the author decided to use the first one giving the fact that it is the most commonly used in engineering problems and which presents better behaviours for a bigger variety of flows [5]. The second choice is also popular in performing CFD computations, once this model can be integrated near a wall without the aid of wall functions [5].

The final goal of this study is to compare the behavior of each turbulence model when studying the performance of annular combustors similar to the most popular turbofan engine's.

1.3 Task Overview

In the first chapter, the author introduces his work by manifesting his motivation behind the development of a study with the CFM56-3 annular combustor chamber. Current issues are presented and how they are tending for the next decades, as well as the present-day resources that can be exploited to leverage this tendencies. The fundamental goals are proposed, as well as the main drivers that will conduct the study. Historical and bibliographic data is reviewed in order to have a context about the subject and its relevance nowadays.

The second chapter approaches the main topics needed to better understand this work. The author introduces the combustion notions, the CFM56-3 engine and the *Standard* k-ε and the

Standard k-ω turbulence models, as they are the fundamental concepts needed to develop the present analysis.

In the third chapter, the author presents the case setup. Here, all the parameters used on the simulations are set: applications, materials, boundary conditions, initial conditions, physical models and grid control.

The final chapter presents the numerical results of the CFD simulation. Outputs are described in detail and discussed. The chapter ends with the conclusions of this study and possible future work proposals.

1.4 Historical Review

Boussinesq performed the first attempts to develop a mathematical description of the turbulent stresses back in 1877, by introducing the eddy viscosity concept [6]. Later, in 1895, Reynolds published his research on turbulence with the time-averaged Navier-Stokes equations [7]. However, neither of the authors tried to solve this equations in any type of systematic way. In 1904, Prandtl discovers the boundary layer, which brought much more information regarding the physics of viscous flow [8]. Later, he presents the concept of the mixing-length model that established an algebraic relation for the turbulent stresses [9]. This model is now also known as zero-equation model.

Twenty years later, Prandtl came out with the first one-equation model by considering the effects of flow history, stating that the eddy viscosity depended on the turbulent kinetic energy, k [10]. This was a more realistic mathematical model, in which a differential equation was solved to approximate the exact equation for k. Also, in 1942, Kolmogorov proposed the first complete turbulence model, taking into account the turbulent kinetic energy, k, and considering a new parameter, regarding the rate of dissipation of energy per unit volume and time, ω. This model consisted in solving a differential equation for ω, similarly to the solution for k. Named k-ω, it used reciprocal of ω as the turbulence time scale and the quantity $k^{1/2}/\omega$ as the turbulence length scale [11]. This model remained virtually until the emergence of computing capacity, due to the complexity required to solve nonlinear differential equations.

In 1951, Rotta used a new approach named second-order or second-moment closure, which took the Boussinesq approximation in turbulence models to solve for the Reynolds stresses, incorporating non-local and history effects, such as streamline curvature and body forces. It was a seven-equation model, using one equation for turbulence length scale and six for the Reynolds stresses. Once again, its use remained not practical until the computer technology evolved [12].

By the 1960's, along with the computer capabilities development, these four classes of turbulence models evolved. Regarding zero-equation models, Van Driest introduced in 1956 a viscous damping correction for the mixing-length model, which is still used in the majority of the modern models [13]. In 1974, Cebeci and Smith refined the concept of mixing-length when used with attached boundary layers [14]. By 1978, Baldwin and Lomax also suggested a different algebraic zero-equation model which allowed to define a turbulence length scale from the shear-layer thickness more easily [15].

Concerning the one-equation models, they didn't have much success, despite being much simpler than two-equation models. Bradshaw, Ferriss, and Atwell, however, formulated a model [16] which was tested against the latest experimental data at the 1968 Turbulent Boundary Layers Conference, in Stanford and is still used as it can be easily solved numerically. In turn, after Kolmogorov's k-ω model, Daly and Harlow, in 1970 [17], and Launder and Spalding, in 1972 [18], extended the study in two-equation models, giving rise to the k-ε model in 1974, in which ε is the dissipation rate of turbulent kinetic energy [19]. Also, in 1970, Saffman proposed a k-ω model, which revealed some advantages by integrating through the viscous sublayer and in flows with adverse pressure gradients [20]. Regarding second-order closure models, they do not have the same popularity because of their complexity. Notable studies for this class of models have been done though. For instance, Donaldson and Rosenbaum in 1968 [21] and Launder, Reece and Rodi in 1975 [22]. Also, other authors such as Lumley in 1978 [23], Speziale in 1985 [24] and 1987 [25] and Reynolds in 1987 [26] brought more mathematical rigor to the model formulation.

1.5 Bibliographic Review

Turbulence

Almost all fluid flows present in our daily life are turbulent. We can find them around cars, airplanes, buildings or in the locomotion of water, land and air living beings. Flows in rivers, oceans and atmosphere are large scale examples. Even the blood in the aorta is occasionally turbulent. A technical example is the flow and combustion of piston engines and gas turbine, which are highly turbulent and is used as a plus to help the mixing of fuel with oxidant for a more efficient combustion. There is no specific definition for turbulence. Peter Bradshaw, in *An introduction To turbulence and its Measurements* states that "Turbulence is a three-dimensional time-dependent motion in which vortex stretching causes velocity fluctuations to spread to all wavelengths between a minimum determined by viscous forces and a maximum determined by the boundary conditions of the flow. It is the usual state of fluid motion except at low Reynolds numbers" [27]. Although we can not have a concrete definition for turbulence, it has a number of characteristic features:

- **Irregularity** - One of its characteristics is about disorder, randomness. Turbulent flow is chaotic and consists of a spectrum of different scales. Their size can be found by the order of the flow geometry. It's in the end of the spectra, that the smallest scales are found, which are by viscous forces (stresses) dissipated into internal energy. Even though turbulence is chaotic it is deterministic and is described by the Navier-Stokes equations [28];
- **Diffusivity** - The diffusivity of the turbulence provokes rapid and efficient mixing and increases the exchange of momentum, heat and mass [29];
- **Large Reynolds numbers** - Turbulent flow occurs at high-Reynolds number. This is also a necessary condition for the transition from a laminar to turbulent flow. However, it is not the only one, once it is needed a perturbation, which can be amplified to trigger the turbulence;
- **Three-Dimensional vorticity fluctuations** - Turbulent flow is rotational and three-dimensional, characterized for its high levels of fluctuating vorticity [29];
- **Dissipation** - Turbulent flow is always dissipative. The mean flow transfers energy to the larger scales, which transfer their kinetic energy to the smaller ones, and so on, until it is transformed into internal energy. This process is called energy cascade. Turbulence needs a continuous supply of energy to compensate this viscous losses. Turbulence decays as soon as energy is not supplied;
- **Continuum** - Even the smaller scales occurring in a turbulent flow flow are ordinarily far larger than any molecular length scale. Turbulence is a continuum phenomena and is governed by the equations of fluid mechanics.

"Turbulence is not a feature of fluids, but of fluid flows" [29]. The molecular properties of the fluid do not control most of its turbulent flow characteristics. Giving the fact that the equations of motions are non-linear, each individual flow pattern has different characteristics, associated with its initial and boundary conditions. No general solution of Navier-Stokes equations is known, thus turbulence is considered an unsolved phenomena of physics. This means that there is no model that describes the emergence and behaviour of turbulence for every situation. Because of the technical importance of turbulence, models based on correlations of particular experimental data have been developed to a large extent [28].

Turbulence Modeling

The study of computational fluid dynamics (CFD), specifically the theoretical analysis and prediction of turbulence, has been the fundamental problem of fluid dynamics in the past decades. Due to its chaotic nature and unpredictability, time averaged forms of the governing equations have been applied. Besides, for most of engineering applications, it is unnecessary to resolve the details of the turbulent fluctuations, however, it is important to know how turbulence affect the mean flow. Turbulence modeling give use to semi-empirical mathematical models for the calculation of unknown correlations [5]. Nowadays, there is a wide scope of turbulence models, although, CFD turbulence analysis can be performed through three different approaches:

1) Direct Numerical Simulation (DNS);
2) Large Eddy Simulation (LES);
3) Reynolds-Averaged Navier-Stokes (RANS).

All approaches have their own applications (see Fig. 1.1) and limitations, as will be described in detail further ahead in this work. For example, Large Eddy Simulation models have failed to provide solutions for most flows of engineering relevance due to excessive computing power requirements for wall-bounded flows [5]. On the other hand, despite RANS models showing their strength for wall-bounded flows, the performance is much less uniform for free shear flows [30]. With the intention of overcoming the shortcomings of both, hybrid RANS/LES approaches are also currently under development, which incorporate aspects of both forms of turbulence modeling [31]. With this approach, large eddies are only resolved away from walls and the wall boundary layers are entirely covered by a RANS model (e.g. Detached Eddy Simulation – DES or Scale-Adaptive Simulation – SAS) [30].

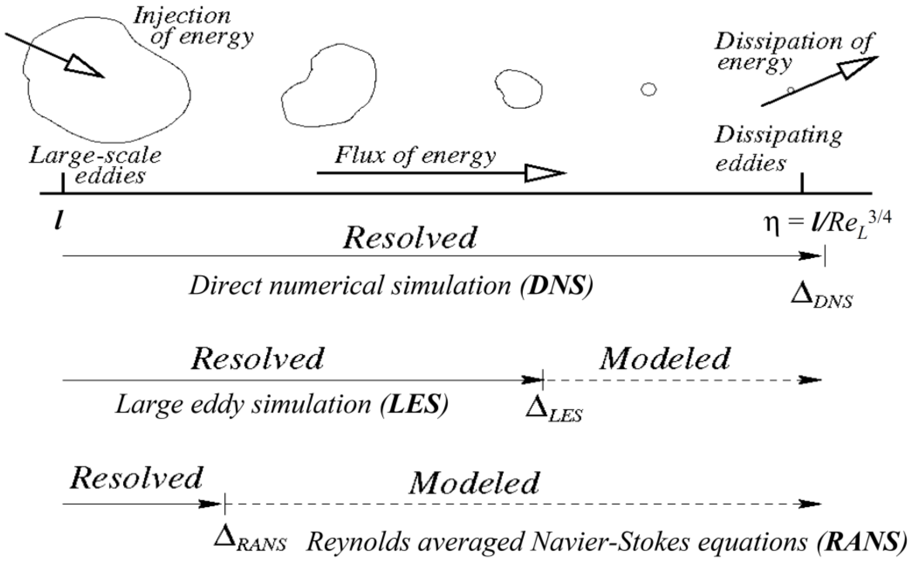

Figure 1.1: Turbulence modelling approaches and their applications [32].

Direct Numerical Simulation

In DNS, no modelling is required besides de Navier-Stokes equations, as it consists in solving them numerically by resolving all scales down to the scale of viscous dissipation. DNS data is considered to be an excellent substitute for exact, analytic solutions of the Navier-Stokes equations, although, in order to obtain solutions for moderately high Reynolds numbers, it requires weeks of computing time on today's largest supercomputers. For example, to achieve the Reynolds numbers of a typical atmospheric boundary layer flow ($Re = 10{,}000$), it would require a 10^8-fold increase in computing power over today's largest computers [33].

Large Eddy Simulation (LES)

As mentioned above, the Navier-Stokes equations can be used to simulate turbulent flows. However, for high Reynolds numbers, the computational grid needed to allow the smallest turbulent length scales to be realized (Kolmogorov Scales[1]) and the computational time step to simulate the highest frequencies of the turbulent spectrum, would be prohibitive. Large eddy simulations (LES) were developed to extend the simulation of unsteady flows beyond DNS [31]. LES computation main goal is to resolve a DNS equivalent solution for the large-scale turbulence on a much coarser grid than is required for DNS. In LES the large scale motions (large eddies) of turbulent flow are computed directly and only small scale motions (sub-grid scale) are modelled, which results in a significant reduction in computational cost compared to DNS [34]. In order to directly compute large eddies, LES applies a low-pass spatial filter to the instantaneous conservative equations. The filtered equations for conservation of mass and momentum in a Newtonian incompressible flow can be written as shown in equations 1.1, 1.2, 1.3 and 1.4 [34].

$$\partial_i \overline{u_i} = 0 \tag{1.1}$$

$$\partial_t(\rho\overline{u_i}) + \partial_j\left(\rho\overline{u_i}\,\overline{u_j}\right) = -\partial_i\overline{p} + 2\partial_j\left(\mu\overline{S_{ij}}\right) - \partial_j\left(\tau_{ij}\right) \tag{1.2}$$

$$\overline{S_{ij}} = \frac{1}{2}\left(\partial_i\overline{u_j} + \partial_j\overline{u_i}\right) \tag{1.3}$$

$$\tau_{ij} = \rho\left(\overline{u_i u_j} + \overline{u_i}\,\overline{u_j}\right) \tag{1.4}$$

where $\bar{u}_i$ is the filtered velocity, $\bar{p}$ is the filtered pressure, $\bar{S}_{ij}$ is the filtered, or resolved scale strain rate tensor and τ_{ij} is the unknown sub-grid scale stress tensor, which represents the effects of the small scale motions on the resolved fields, and needs to be modelled so the above governing equations can be solved. Different LES models use different methods to calculate the sub-grid stress tensor and most of them, similarly to RANS approach, use the eddy-vicosity concept, also called the Boussinesq assumption[2]. Once this assumption is

---

[1] Komogorov Scales are explained in page 12

[2] The Boussinesq Hypothesis is approached in page 12

applied, the sub-grid eddy-viscosity needs to be determined [34]. As LES approach will not be used in the present work, only the most basic model to calculate the turbulent eddy viscosity will be presented, the one originally proposed by Smagorinsky (see Eq. 1.5, Eq. 1.6 and Eq. 1.7) [35].

$$\mu_t = \rho(C_S\bar{\Delta}) \tag{1.5}$$

$$S = \left(2\bar{S}_{ij}\bar{S}_{ij}\right)^{\frac{1}{2}} \tag{1.6}$$

$$\Delta = (\Delta x \Delta y \Delta z) \tag{1.7}$$

where C_S is Smagorinsky constant which depends on the type of the flow.

In general, LES modeling is believed to allow for better fidelity than RANS methods, at a lower computational cost compared to DNS [36]. Large Eddy Simulation captures the large eddies in full detail directly whereas they are modelled in the RANS approach. Since large eddies contain most of the turbulent energy and are responsible for most of the momentum transfer and turbulent mixing, some authors consider LES more accurate than the RANS approach. Moreover, the small scales tend to be more isotropic and homogeneous than the large ones, hence, modelling the SGS motions can be easier than modelling all scales within a single model as in the RANS modelling. [34] However, despite being less expensive computationally than DNS, LES still demands an excessive computing power for wall-bounded flows, due to its grid refinement requirements, which for engineering purposes usually becomes unfeasible [30]. Besides it is also considered to be too dissipative, which is not good for transition simulation) [34].

Reynolds-Averaged Navier-Stokes (RANS)

In RANS modelling, turbulence is modelled using the Reynolds Averaged Navier Stokes (RANS) equations, which are derived by averaging the Navier-Stokes and continuity equations. The main goal of RANS approach is to model the Reynolds Stresses which describe the effects of the turbulent fluctuations of pressure and velocities [37]. For that purpose, different models are available, from relatively simple to more complex methods. Beginning with zero-equation models, such as the Mixing-length Model, one-equation models, for instance the Spalart-Almaras, two equation models, such as k-ε (standard, RNG, realizable), or the k-ω (standard, SST), until second order models with more equations and much more complexity involved. In the present work, the k-ε Standard and k-ω are used and will be approached in chapter 2.

As mentioned before, RANS approach starts by averaging the Navier-Stokes and continuity equations. Considering the incompressible Navier-Stokes equations in conservation form (Eq. 1.8 and Eq. 1.9) [38]:

$$\frac{\partial u_i}{\partial x_i} = 0 \tag{1.8}$$

$$\rho\frac{\partial u_i}{\partial t} + \rho\frac{\partial}{\partial x_j}\left(\bar{u}_j\bar{u}_i\right) = \frac{\partial p}{\partial x_i} + \frac{\partial}{\partial x_j}\left(2\mu s_{ij}\right) \tag{1.9}$$

where the strain-rate tensor s_{ij} is given by Eq. 1.10:

$$s_{ij} = \frac{1}{2}\left(\frac{\partial u_i}{\partial x_j} + \frac{\partial u_j}{\partial x_i}\right) \tag{1.10}$$

By the application of equation 1.8, the equations of motion can be written as seen in Eq. 1.11 [38]:

$$\rho\frac{\partial u_i}{\partial t} + \rho\bar{u}_j\frac{\partial u_i}{\partial x_i} = -\frac{\partial p}{\partial x_i} + \mu\frac{\partial^2 u_i}{\partial x_i \partial x_j} \tag{1.11}$$

Then, RANS approach employs the so-called Reynolds decomposition, where the flow variables velocity and pressure are divided in two parts. One time-averaged part, which is independent of time (when the mean flow is steady), and one fluctuating part [38], as shown in Eq. 1.12:

$$u_i = U_i + u_i' \text{ and } p = P + p' \tag{1.12}$$

where the mean and fluctuating parts satisfy Eq. 1.13 and Eq. 1.14 [38]:

$$\overline{u_i} = U_i \text{ and } \overline{u_i'} = 0 \tag{1.13}$$

$$\overline{p} = P \text{ and } \overline{p'} = 0 \tag{1.14}$$

with the bar denoting the time average. This set of equations generated describe the average flow field, which means that any propriety becomes constant over time. The decomposed equations will describe an average and not the exact turbulent flow field [39].

Using the Reynolds decomposition (Eq. 1.12) in the governing equations 1.8 and 1.9 results in the Reynolds Averaged Navier-Stokes (RANS) equations, as shown in Eq. 1.15 and 1.16 [38]:

$$\frac{\partial U_i}{\partial x_i} = 0 \tag{1.15}$$

$$\rho \frac{\partial U_i}{\partial t} + \rho \frac{\partial}{\partial x_j}\left(U_j U_i\right) = \frac{\partial P}{\partial x_i} + \frac{\partial}{\partial x_j}\left(2\mu S_{ij} - \rho \overline{u_i' u_j'}\right) \tag{1.16}$$

where S_{ij} is the mean strain-rate sensor of Eq. 1.17 [38]:

$$S_{ij} = \frac{1}{2}\left(\frac{\partial U_i}{\partial x_j} + \frac{\partial U_j}{\partial x_i}\right) \tag{1.17}$$

The RANS equations are similar to the instantaneous Navier-Stokes equations. Although, the dependent variables in RANS equations are the mean velocities and mean pressures, instead of the instantaneous values. Besides, the decomposition results in an unclosed term in the transport equations, the Reynolds stress tensor τ_{ij}, which represents the effect of turbulent fluctuations on the mean flow, give by Eq. 1.18 [37]:

$$\tau_{ij} = -\rho \overline{u_i' u_j'} \tag{1.18}$$

By decomposing the instantaneous variables into mean and fluctuating parts, we have introduced three more unknown quantities (one for each direction). However, we have not gain any additional equations, meaning our system is not yet closed. To close the system, it must be found enough equations to solve the unknowns [38]. Different RANS models use different methods to solve RANS equations and are often divided in two classes of models: Eddy viscosity models, which use the turbulent viscosity hypothesis (or Boussinesq hypothesis) to approximate the Reynolds stress tensor as a function of the eddy-viscosity and the mean-stress-tensor S_{ij}. On the other hand, second order closure models solve modelled differential equations for the Reynolds [37]. A diagram about the most common RANS turbulence models is shown above, in order of increasing complexity [39]:

- First Order Models
    - Zero-Equation Models
        - Mixing-Length Model
    - One-Equation Models
        - k-model

        - μ_t-model
    - Two-Equation Models
        - k-ε (standard, RNG, realizable, Low-Re)
        - k-ω (standard, SST)
- Second Order Models
    - Algebraic Stress Models (ASM)
    - Reynolds Stress Models (RSM)

In RANS modelling, the computing resources for reasonably accurate flow computations are modest, so this approach has been the most explored. For most engineering purposes it is not necessary to resolve in detail the turbulent fluctuations, once the time-averaged properties of the flow satisfy the CFD users needs [40]. Each RANS model has its own advantages and disadvantages. In chapter 2, the benefits and limitations of the Standard k-ε and the Standard k-ω models will be explored.

The Boussinesq Hypothesis

The Boussinesq hypothesis comes from a very old proposal for modeling the turbulent or Reynolds stresses. In this approach, the turbulent eddies are treated and analyzed in a similar way to the molecules in kinetic theory. The concept assumes that, in analogy to the viscous stresses in laminar flows, the turbulent stresses are proportional to the mean velocity gradient, given by Eq. 1.19 [38]:

$$-\overline{u_i{}'u_j{}'} = 2\nu_T S_{ij} - \frac{2}{3}k\delta_{ij} \tag{1.19}$$

where ν is the kinematic eddy viscosity. However, contrary to the molecular viscosity, the turbulent viscosity is not a propriety of the fluid, but a propriety of the flow. That means it strongly depends on the state of turbulence. So ν may be significantly different from one point of the flow to another and from flow to flow too [5].

Kolmogorov Scales

In order to properly select a computational grid spacing and time step for a given problem, it is useful to quantify the range of length and time scales associated with a turbulent flow [31] Turbulent scales are distributed over a range of scales, which extends from largest scales, that interact with the mean flow, to the smallest scales, where dissipation occurs [41]. The interaction between the scales of various scales passes energy sequentially from the larger eddies to the smaller ones in a process called Energy Cascade (see Fig. 1.2) [42].

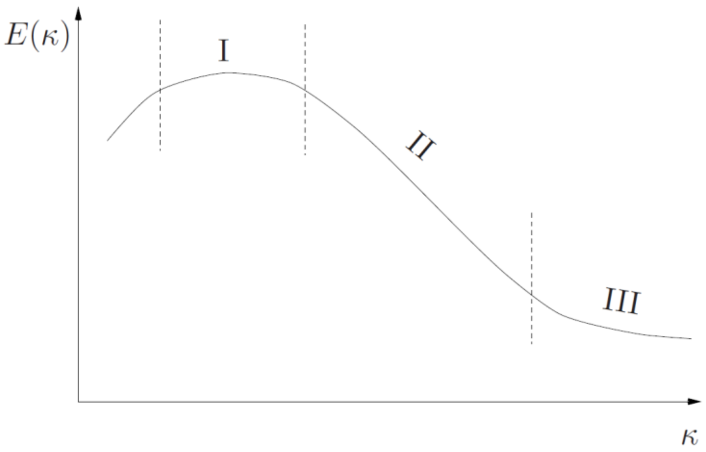

Figure 1.2 Energy cascade spectrum [41]

The Energy Cascade can be divided in three regions, which correspond to [41]:

1) The first region is where the large eddies interact and extract energy from the mean flow. Large eddies carry most of the energy in the Energy Cascade. The turbulent kinetic energy k and turbulent dissipation ε are usually associated with the larger scales of turbulence. From dimensional analysis, the large eddies have length scales and time scales characterized by Eq. 1.20 and 1.21 [31]:

$$L = \frac{k^{\frac{3}{2}}}{\varepsilon} \tag{1.20}$$

$$T = \frac{k}{\varepsilon} \tag{1.21}$$

2) The second region, also named Inertial subrange, is a “transport” region in the Energy Cascade. The energy comes from the large eddies at the lower part of this region and is given off to the dissipation range, at its higher part. Kolmogorov Spectrum Law states that if the flow is fully turbulent, the energy spectra should exhibit a $-5/3$-decay [41].
3) The third region is the smallest level of scales, where the energy is lost to viscous dissipation [28]. For turbulent flows at sufficiently high Reynolds number, the small-scale turbulent motions ($l \ll l_0$) are statistically isotropic[3], i.e. does not have a preferred orientation. Besides, at this level, the statistics of small-scale motions ($l < l_{EI}$) have a universal form that is uniquely determined by ν and ε[4]. Giving this two

---

[3] Kolmogorov’s hypothesis of local isotropy [43]
[4] Kolmogorov’s first similarity hypothesis [43]

parameters, unique length, velocity and time scales can be formed (to within multiplicative constants). These are the so-called Kolmogorov Scales and are described in Eq. 1.22, Eq. 1.23 and Eq. 1.24 [43]:

$$\eta \equiv (\nu^3/\varepsilon)^{1/4} \tag{1.22}$$

$$u_\eta \equiv (\varepsilon\nu)^{1/4} \tag{1.23}$$

$$\tau_\eta \equiv (\nu/\varepsilon)^{1/2} \tag{1.24}$$

The length scale is the smallest scale in a turbulent flow [28]. To ensure the turbulence universal equilibrium, the dissipation rate must be equal to the energy transfer from the largest scales, where energy is injected. By knowing the energy input in a certain flow it is thus possible to determine the Kolmogorov Scales [28].

Wall Bounded Flows

As most of engineering problems, the present work involves a constrained flow by solid boundaries. The presence of a a wall highly affects turbulent flow since the Reynolds number decreases as the wall is approached, the mean velocity changes from zero at the wall to its stream value in order to satisfy the no-slip condition, implying large mean velocity gradients. Besides, the impermeability condition also blocks the normal fluctuations. Some turbulence models, such as the k-ε do not perform well in the area close to the wall. Usually, near wall regions are treated by two different ways. One is to integrate the turbulence to the wall. Turbulence models are modified to enable the viscosity-affected region to be resolved with all the mesh down to the wall, including the viscous sublayer [44]. The grid needs to be sufficiently fine so that the sharp gradients prevailing there are resolved [41]. Often, when computing complex three-dimensional flow, this approach leads to requirement of abundant mesh number, which means a substantial computational resource is needed [44]. The other way is to use so-called wall functions, which are empirical equations used to satisfy the physics of the flow in the near wall region [44]. The assumption that the flow near the wall has the characteristics of a flow in a boundary layer is often not true at all. Nevertheless, given the computational cost to resolve the viscosity-affected region, it is often preferable to use wall functions, and still have relatively accurate results under certain conditions [41]. When using modified a low Reynolds turbulence model to solve the near-wall region the first cell center must be placed in the viscous sublayer (preferably $y^+ = 1$). In turn, while using wall functions approach there is no need to resolve the boundary layer, which yields to a significant reduction of the mesh size and the computational domain. The first cell center needs to be placed in the log-law region [44].

In the near-wall region, an appropriate velocity scale for flow is the friction velocity, defined by Eq. 1.25 [45]:

$$u_* = \sqrt{\frac{\tau_w}{\rho}} \tag{1.25}$$

where τ_w is the wall shear stress and ρ is the density at the wall. Considering this velocity scale, a dimensionless velocity u^+ and dimensionless distance to the wall y^+ are defined by Eq. 1.26 and Eq. 1.27, respectively[45]:

$$u^+ = \frac{u}{u_*} \tag{1.26}$$

and

$$y^+ = \frac{y \times u_*}{\nu} \tag{1.27}$$

where u is the velocity component parallel to the wall, y is th normal distance to the wall and ν is the kinematic viscosity.

A near-wall region can be divided into three regions (see Fig 1.3), excluding the outter region (or defect layer), where only turbulent stresses dominates and the molecular viscosity can is negligible: the inner layer, also named viscous sublayer ($y^+ < 5$), where the viscosity plays a dominant role in momentum transport [37] so it can be assumed that the fluid shear stress is equal to the wall shear stress τ_w. In the viscous sublayer, stress decide the flow and the velocity profile is linear [44], given by Eq. 1.28:

$$u^+ = y^+ \tag{1.28}$$

In turn, in the log region turbulence stress dominate the flow [44] and the velocity profiles have been shown to follow the logarithm of the distance to the wall [37], defined by equation 1.29:

$$u^+ = \frac{1}{\kappa}\ln(y^+) + B \tag{1.29}$$

where κ is the von Karman constant ($\kappa = 0.42$) and B is an additional constant which depends on the roughness of the wall [5].

Lastly, in the buffer layer viscous and turbulent stresses are of similar magnitude. Giving the fact that the velocity profile in this region is complex and not well defined, wall functions avoid the first cell center to be located in this region.

The set of equations describing the velocity profile in the inner region is called Law of the wall.

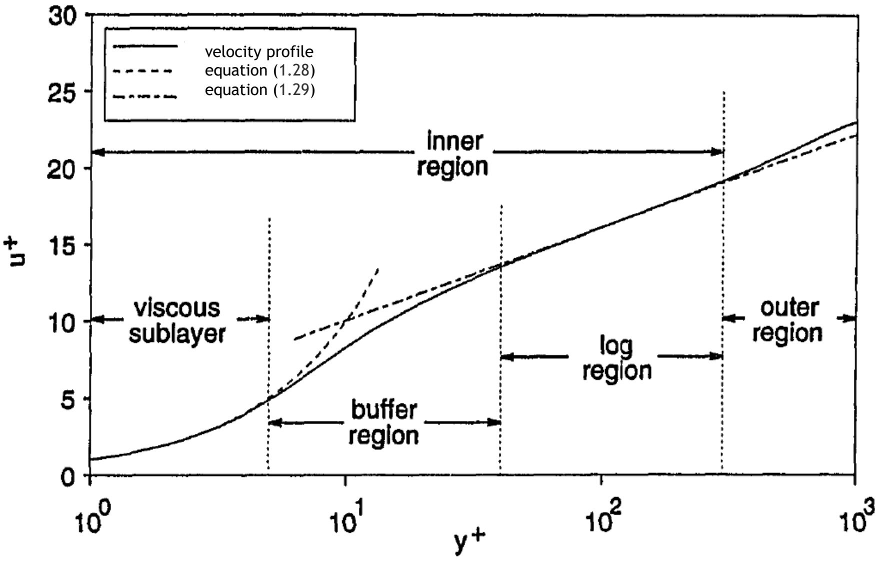

Figure 1.3: Typical turbulent boundary layer velocity profile [45].

Chapter 2

Two-equation models

In order to take any conclusions about the models performance in this study, it is important to understand the physical assumptions behind them. In this chapter, both standard k-ε and standard k-ω models will be presented, the major implicit assumptions needed to formulate their equations, their influence in the results and a final comparisation between them.

Two-equation models have been very popular for a wide range of engineering analysis and research [5]. There are numerous of these models in the literature. Most of them solve a transport equation for turbulent kinetic energy, k, and a second transport equation that allows a turbulent length scale to be determined. The most common forms of the second transport equation solve for turbulent dissipation ε or turbulent specific dissipation ω [31]. By specifying this two variables, these models are complete, i. e., no prior knowledge of the turbulence structure is needed to predict properties for a given flow [46].

In spite of appearing to apply to a wide range of flows, it is prudent to understand the implicit assumptions made in formulating a two-equation model. The first major assumption is that the turbulent fluctuations are locally isotropic or equal. This is true for the smaller eddies at high Reynolds numbers. However, the large scales are in a state of steady ansiotropy due to the strain rate of the mean flow, so the fluctuations are often of the same magnitude. This assumption implies that the normal Reynolds stresses are equal at a point in the flowfield [5]. Another one is the assumption of local equilibrium, where turbulent production and dissipation terms, given in the k-equation, are approximately equal locally [5]. Thus, two-equation models are to some degree limited to flows in which this assumptions are not grossly violated. Tough somewhat restricted, when applied to appropriate cases, these models can be used to give results within engineering interest.

2.1 k-ε Model

The k-ε has been the most common two-equation model used in the past three decades [37] and is available in most of commercial CFD softwares [47]. In this model, an equation for the dissipation ε is obtained from the ε exact equation by taking the moment of Navier-Stokes equations (Eq. 2.30) [37].

$$\overline{2\nu \frac{\partial u'_i}{\partial x_j} \frac{\partial}{\partial x_j}[N(u_i)]} \tag{2.30}$$

where $N(u_i)$ is the Navier-Stokes operator, defined by Eq. 2.31:

$$N(u_i) = \rho \frac{\partial u_i}{\partial t} + \rho u_k \frac{\partial u_i}{\partial x_k} + \frac{\partial p}{\partial x_i} - \mu \frac{\partial^2 u_i}{\partial x_k \partial x_k} \tag{2.31}$$

After a tedious manipulation, the exact equation of ε can be written as Eq. 2.32:

$$\begin{aligned} \frac{\partial \varepsilon}{\partial t} + U_j \frac{\partial \varepsilon}{\partial x_j} = -2\nu\left[\overline{u'_{i,j}u'_{i,k}} + \overline{u'_{k,i}u'_{k,j}}\right]\frac{U_i}{\partial x_j} - 2\nu\overline{u'_k u'_{i,j}}\frac{\partial^2 U_i}{\partial x_j \partial x_k} \\ -2\nu\overline{u'_{i,k}u'_{i,m}u'_{k,m}} - 2\nu^2\overline{u'_{i,km}u'_{i,km}} \\ +\frac{\partial}{\partial x_j}\left[\nu\frac{\partial \varepsilon}{\partial x_j} - \nu\overline{u'_j u'_{i,m}u'_{i,m}} - 2\frac{\nu}{\rho}\overline{p'_m u'_{j,m}}\right] \end{aligned} \tag{2.32}$$

This equation involves many new unknown second and third order correlations of fluctuating velocities, pressure and velocity gradients. As mentioned before, the k-ε model is based on the ε exact equation (2.32). As the dissipation of the turbulent kinetic energy happens in the smallest eddies, where the kinetic energy of the small motions are converted to thermal energy by molecular viscosity, this equation describes the processes of small eddies [37]. However, what is actually needed in the model is a length or time scale relevant to the large, energy containing eddies [5]. Therefore, we use a modelled equation to describe the rate of energy transferred from the large eddies to the small eddies. This is appropriate once the rate of dissipation to heat is set by the rate at which energy is transferred along the energy cascade. Standard k-ε model can be described with equations 2.33, 2.34, 2.35 and 2.36 [37]:

Turbulent Kinetic Energy:

$$\frac{\partial k}{\partial t} + U_i \frac{\partial k}{\partial x_i} = \tau_{ij} \frac{\partial U_i}{\partial x_j} - \varepsilon + \frac{\partial}{\partial x_j}\left[(\nu + \nu_T/\sigma_k)\frac{\partial k}{\partial x_j}\right] \tag{2.33}$$

Dissipation Rate:

$$\frac{\partial \varepsilon}{\partial t} + U_i \frac{\partial \varepsilon}{\partial x_i} = C_{\varepsilon 1} \frac{\varepsilon}{k} \tau_{ij} \frac{\partial U_i}{\partial x_j} - C_{\varepsilon 2} \frac{\varepsilon^2}{k} + \frac{\partial}{\partial x_j}\left[(\nu + \nu_T/\sigma_\varepsilon)\frac{\partial k}{\partial x_j}\right] \tag{2.34}$$

Eddy Viscosity:

$$\nu_T = C_\mu k^2/\varepsilon \tag{2.35}$$

Closure Coefficient and Auxiliary Relations:

$$C_{\varepsilon 1} = 1.44, \quad C_{\varepsilon 2} = 1.92, \quad C_\mu = 0.09, \quad \sigma_k = 1.0, \quad \sigma_\varepsilon = 1.3, \tag{2.36}$$

$$\omega = \varepsilon/(C_\mu k), \quad l = C_\mu k^{2/3}/\varepsilon \tag{2.36}$$

2.2 *k*-*ω* Model

Wilcox's k-ω model is another two-equation model very popular in performing CFD computations [47]. Unlike k-ε, which solves for the dissipation of kinetic energy, the k-ω solves for only the rate at which that dissipation occurs ($\omega = \varepsilon/k$). We can also interpret it as the inverse of the time scale on which dissipation occurs [5]. Although this dissipation happens at molecular level, its actual rate is set by the rate of transfer of energy down the eddy spectrum, consequently, ω is set by the large-scale motions, so it is closely related to the mean-flow properties [37]. Unlike for the standard k-ε, the equation for ω was not derived from an exact equation, but has rather been formulated based on physical reasoning, taking into account the processes normally governing the transport equation, such as convection, diffusion, production, and destruction of dissipation [5]. The first two-equation model was a k-ω model developed by Kolmogorov in 1942 [11], however, the most popular k-ω is that of Wilcox, commonly referred as the standard k-ω and is described by Eq. 2.37, Eq. 2.38, Eq. 2.39 and Eq. 2.40 [37]:

Turbulent Kinetic Energy:

$$\frac{\partial k}{\partial t} + U_i \frac{\partial k}{\partial x_i} = \tau_{ij} \frac{\partial U_i}{\partial x_j} - \beta^* k\omega + \frac{\partial}{\partial x_j}\left[(\nu + \sigma^* \nu_T)\frac{\partial k}{\partial x_j}\right] \tag{2.37}$$

Specific Dissipation Rate:

$$\frac{\partial \omega}{\partial t} + U_i \frac{\partial \omega}{\partial x_i} = \alpha \frac{\omega}{k} \tau_{ij} \frac{\partial U_i}{\partial x_j} - \beta\omega^2 + \frac{\partial}{\partial x_j}\left[(\nu + \sigma \nu_T)\frac{\partial \omega}{\partial x_j}\right] \tag{2.38}$$

Eddy Viscosity:

$$\nu_T = k/\omega \tag{2.39}$$

Closure Coefficient and Auxiliary Relations:

$$\begin{gathered} \alpha = 13/25, \quad \beta = \beta_o f_\beta, \quad \beta^* = \beta_o^* f_{\beta^*}, \quad \sigma = 1/2, \quad \sigma^* = 1/2, \\ \beta_o = 9/125, \quad f_\beta = 1.0, \quad \beta_o^* = 9/100, \quad f_{\beta^*} = 1.0, \\ \varepsilon = \beta^* \omega k, \quad l = k^{1/2}/\omega \end{gathered} \tag{2.40}$$

The determination of the closure coefficients for these two-equation models are obtained in a systematic manner, applying a semi-empirical procedure and optimisation. This determination is not rigorous, once the models involve many assumptions and arguments based on physical reasoning. Thus, the approach used to determine the closure coefficients is to set the values in such a way that the model obtains reasonable agreement with experimentally observed properties of turbulence. This method is subject to a high degree of presumption and the values set for a constant from one application, may not be necessarily suitable for a wide range of turbulent flows [5].

2.3 Comparisation of the Two-equation Models in diverse applications

For free shear flows, such as flows given by jets, wakes and mixing layers, both models perform reasonably well. Predictions made by the k-ε model for these flows have shown to be within 30% of DNS predictions for the far wake and round jets, 15% for the mixing layer and 5% for the plane jet. In turn, the k-ω model has shown to make predictions somewhat even closer for each of the mentioned cases [5]. However, k-ω model has a large dependence on the free stream boundary condition for ω. This sensitivity can lead to inaccurate solutions, thus ω needs to be appropriately specified at free stream boundaries [37].

Concerning wall shear flows, in the derivation of the k-ε model, it was assumed that the flow is fully turbulent and the effects of molecular viscosity are neglected. Hence this model in its present form is not capable to solve calculations of the low-Reynolds number flows or wall bounded flows [47]. Thus, k-ε necessitates either a low Reynold modification or the use of wall functions to resolve the near-wall region [5]. On the other hand, k-ω model ensures that, with no viscous damping of the model's closure coefficients, the model equations can be integrated through the viscous sublayer without the aid of wall functions [47]. This model has been shown to reliably predict the law of the wall when the model is used to resolve the viscous sublayer, consequently eliminating the need to use a wall function, except for computational efficiency [5].

Another deficiency of the k-ε is the substantial numerical stiffness near the wall that makes the ε-equation difficult to solve and forces the use of small time steps to account for processes operating over multiple time-scales [37]. Besides, in many flow situations the ω-equation is more numerically stable than the ε-equation, allowing larger time-steps.

Considering a constant incompressible boundary layer at high Reynolds number, both models perform very well predicting values of the friction coefficient and mean velocity within 5%. Although, for incompressible boundary layers with adverse pressure gradients, the k-ε model has shown to be more inaccurate with predictions of 20%, when compared to 5% error of k-ω [5]. This poor performance is believed to result from the ε-equation overprediction of the turbulent length scale, resulting in a high wall shear stress [47]. For this reason, k-ε often predicts a delayed separation or prevent it completely [37].

Generally, neither model is capable of giving quantitatively good results for more complicated flows, such as flows with sudden changes in the mean strain rate, curved surfaces, secondary motions, and separation. However, they may give qualitative results with close agreement with experiments [5].

Chapter 3

Combustion considerations

Combustions and its control are essential to our existence. Approximately 86% of the energy in the world came from consumption sources such as oil, coal and gas (see Fig. 3.1) [2]. If we look at our daily life, we can notice that the heating of our homes, the motion of our cars, aircrafts, ships, even cooking mostly use combustion directly, or indirectly, through electricity that is often generated by burning fossil fuels. The fuels used in combustion can be divided in fossil fuels and biomass. The first ones, such as crude oil derivatives (gasoline, diesel, kerosene, fuel-oil), coal and natural gas come from non-renewable resources, while the seconds can be considered as renewable. The main pollutants resulting from combustion are the carbon monoxide, unburnt hydrocarbons, nitrogen oxides, sulfur dioxide and solid particles, which can cause health problems, smog, acid rain, ozone layer depletion and greenhouse effect.

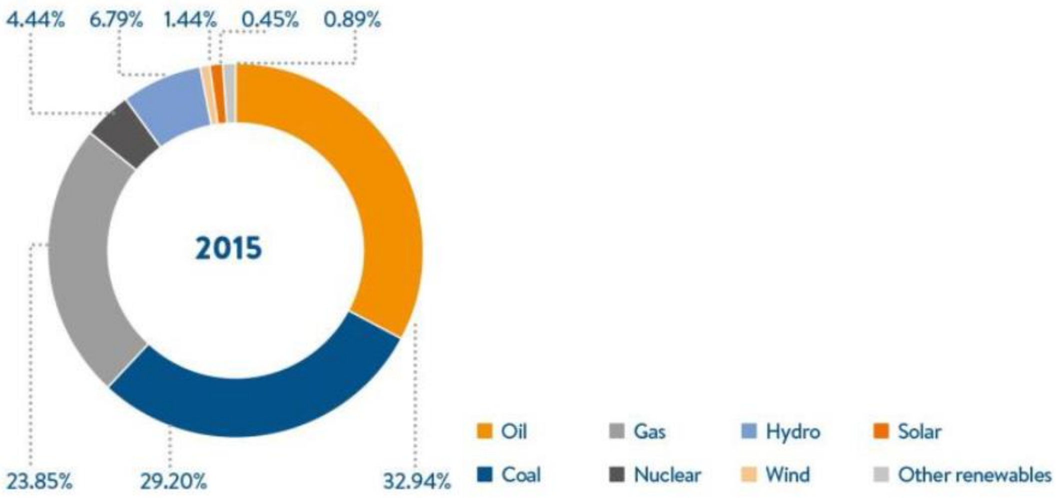

Figure 3.1: Primary energy Comsumption in 2015 [2].

The concept of Combustion is not easy to define. Stephen R. Turns quotes the Webster Dictionary as “rapid oxidation generating heat, or both heat and light” [48]. Other authors, Amable Liñán and Forman A. Williams define combustion science as “the science of exothermic chemical reactions in flows with heat and mass transfer” in *Fundamental Aspects of Combustion* [49], which is believed to be more comprehensive.

Combustion can occur in two different modes: flame and non flame (see Fig. 3.2 and Fig. 3.3). The flame is characterized by a thin reaction zone of intense chemical reaction propagating through the unburned fuel air-mixture. As it moves across the combustion space, the temperature and pressure rise in the unburned gas, where, under certain conditions, rapid oxidation reactions occur: This leads to very rapid non-flame combustion, commonly called autoignition [48].

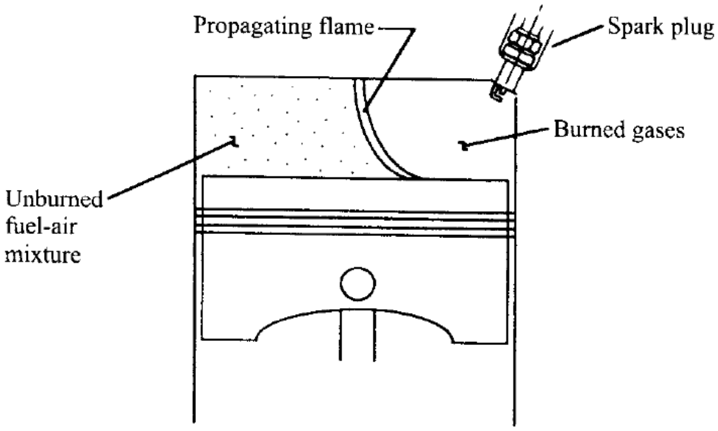

Figure 3.2 Flame mode of combustion in a spark-ignition engine [48].

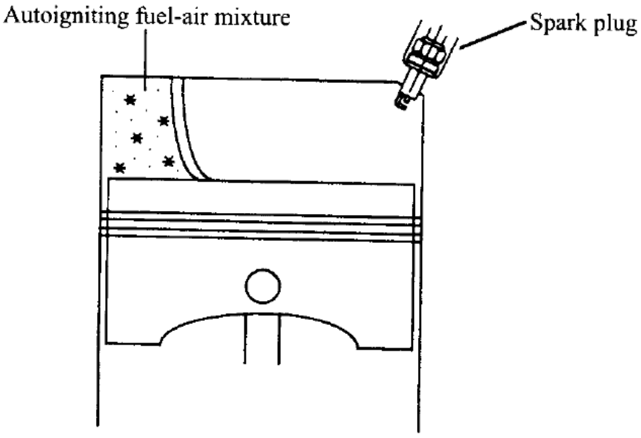

Figure 3.3: Non flame mode of combustion in a spark-ignition engine [48].

Flames can be categorized in two types: premixed flames, which happen when fuel and the oxidizer are mixed at the molecular level before the occurrence of any chemical reaction, usually triggered by a spark; on the other hand, in non-premixed (or diffusion) flames reactants are initially separated and the reaction occurs only at the interface between the fuel and oxidizer, where mixing reactions both take place [5]. While the first type is typical of a gasoline engine, the second is typical of a diesel or a gas turbine engine.

3.1 Stoichiometry

In a combustion process, the chemical composition of the reactive mixture varies over time. The chemical species in the beginning of the process, the reagents, give rise to different final chemical species, the products, by the chemical reaction. The total number atoms of each elements remain the same though. In such a process, the two key reagents are the fuel and de oxidizer. The first is usually a hydrocarbon, whose chemical formula is C_xH_y. The most common oxidizer is the air, which can be considered as an ideal mixture of 21% of O_2 and 79% of N_2 (volumetric), that corresponds to 3,76 N_2 mol per each O_2 mole. The stoichiometric quantity of oxidizer is the just amount necessary to completely burn a quantity of fuel. If any extra quantity of oxidizer is supplied, the mixture is considered lean. Similarly, if the quantity of oxidizer supplied is inferior to the stoichiometric, it results in a rich mixture. The relation for a given hydrocarbon fuel reacting with air is given by Eq. 3.41 and Eq. 3.42:

$$C_nH_m + a(O_2 + 3.76N_2) \rightarrow nCO_2 + \frac{m}{2}H_2O + 3.76aN_2 \tag{3.41}$$

where

$$a = n + \frac{m}{4} \tag{3.42}$$

In Eq. 3.43 we consider Jet-A, kerosene-based ($C_{12}H_{24}$) as the hydrocarbon:

$$C_{12}H_{24} + 18O_2 + 67.7N_2 \rightarrow 12CO_2 + 12H_2O + 67.7N_2 \tag{3.43}$$

Considering the atomic weights of the atoms of Carbon (12,011), Oxygen (15.999) and Hydrogen (1.008), and multiplying by the number of each atoms, we conclude that the kerosene has a molecular weight of 168.24 kg/mol, while O_2 has a molecular weight of 31.998 kg/mol, which for this stoichiometry corresponds to 575.96 kg/mol. This means for each kilogram of fuel, 3.42 kilograms of oxygen are needed. Considering that 21% of air is oxygen, to completely burn a kilogram of fuel, it is needed approximately 16.29 kg of air.

3.2 Absolute Enthalpy, Enthalpy of Formation, Enthalpy of Combustion

Concerning reacting systems, the concept of absolute enthalpy is very important. For any species, we can define an absolute enthalpy, which is the sum of the enthalpy of formation (h_f), related to the energy associated to chemical bonds, with the sensible enthalpy change (Δh_s), associated only with temperature, and given by Eq. 3.44:

$$\bar{h}_i(T) = \bar{h}^{\circ}_{f,i}(T_{ref}) + \Delta\bar{h}_{s,i}(T_{ref})$$

(3.44)

where $\bar{h}_{s,i} \equiv \bar{h}_i(T) - \bar{h}^{\circ}_{f,i}(T_{ref})$

In order to use the equation (3.44), it is necessary to consider the standard reference state for temperature $(T_{ref} = 25°C = 298.15K)$ and pressure $(P_{ref} = P° = 1atm = 101.325Pa)$, according to Chemkin and NASA thermodynamic databases [48].

When the reagents and products of a chemical reaction are at the same reference state, the energy released or absorbed in the chemical reaction is entitled enthalpy of reaction. In combustion reactions, it can be named enthalpy of combustion. Considering a complete combustion process, for the products exit at the same temperature as the reactant enter, heat must consequently be released from the combustor. Taking into account the 1st law of thermodynamics, this amount of energy can be related to the reactant and product absolute enthalpies, as Eq. 3.45 shows:

$$q_{cv} = h_0 - h_i = h_{prod} - h_{reac} \tag{3.45}$$

As a result, the definition of the enthaply of combustion (Δh_R), per mass of mixture, is given by Eq. 3.46:

$$\Delta h_R \equiv q_{cv} = h_{prod} - h_{reac} \tag{3.46}$$

3.3 Adiabatic Flame Temperature

For a certain adiabatic combustion process, where there is no exchange of work and the variation of kinetic and potential energy are despicable, the temperature of the combustion products is called adiabatic flame temperature (T_{ad}) and corresponds to the maximum temperature that can occur in such reaction. However, the temperature of the reaction products is usually inferior due to heat losses, incomplete combustion and dissociation. For any mixture, the maximum T_{ad} occurs at stoichiometric quantities [52]. Two adiabatic flame temperatures can be defined: one concerning constant-pressure combustion and other for constant-volume. Considering the first and assuming a fuel-air mixture which bruns adiabatically, the absolute enthalpy of the reactants at the initial state equals the absolute enthalpy of the products at the final state $(T = T_{ad}, P = 1\ atm)$ as expressed by Eq. 3.47:

$$h_{reac}(T_i, P) = h_{prod}(T_{ad}, P) \tag{3.47}$$

3.4 Combustion Modeling

Combustion is characterized by two phenomena. Transport [of spieces, energy (including radiation) and momentum] and Chemical reactions. If all chemical reactions and spieces are included, the simulation would be impractical due to computer limitations. Since it is not possible to solve combustion directly, models are required.

Many models are designed either for only premixed or for only non-premixed combustion processes. The following are the combustion models available in the software used in this study:

Premixed turbulent combustion models

- Chemical Equilibrium (CEQ)
- G-Equation
- Extended Coherent Flame Model (ECFM)
- Flamelet Generated Manifold (FGM)

Non-premixed turbulent combustion models

- Characteristic Time Combustion (CTC)
- Shell Ignition
- Chemical Equilibrium (CEQ)
- Representative Interactive Flamelet (RIF)
- Extended Coherent Flame Model with the 3Z mixing model (ECFM3Z)

The software used for the numerical analysis of the present study, also contains a detailed chemistry solver, SAGE, which is claimed by the developer to be the most predictive and accurate way to model combustion, ignition and laminar flame propagation. Simplified combustion models are generally less computationally expensive. Though, are still less predictive and may provide acceptable results for only specific application.

All combustion models require good initial conditions and boundary conditions to be accurate. Pressure, temperature and equivalence ratio should be correct at the time of combustion, compression pressure should be correct at the start of injection and trapped mass should also be correct. Besides, sufficient grid resolution is also critical.

Chapter 4

The CFM56-3

The CFM56-3 comes from the CFM56 family, the world's best-seller engine series claimed by its manufacturer, CFM International, to have delivered 30,000 engines up to date, powering single-aisle airplanes for more than 550 operators worldwide, and owning its success for its reliability and performance. The first CFM56-3 engines were designed for Boeing 737-300/400/500 aircraft back in the 1970's. Deriving from the CFM56-2, it is a high bypass ratio engine (5:1), has two spools and axial flow. It can be found in four different versions [50] as shown in table 4.1:

Table 4.1: CFM56-3 versions, thrust and application.

Version	Thrust	Application
CFM56-3-B1	20000 *lb*	B737-300/-500
CFM56-3-B2	22000 *lb*	B737-300/-500
CFM56-3-C1	23500 *lb*	B737-400
CFM56-3-B1 Derated	18500 *lb*	B737-500

The constitution of the engine can be divided in three main parts: low pressure system, high pressure system and accessory drive section. Each part is constituted by numerous components (see Fig. 4.1). In the present work, three main components of high pressure system will be approached, due to its importance for the study.

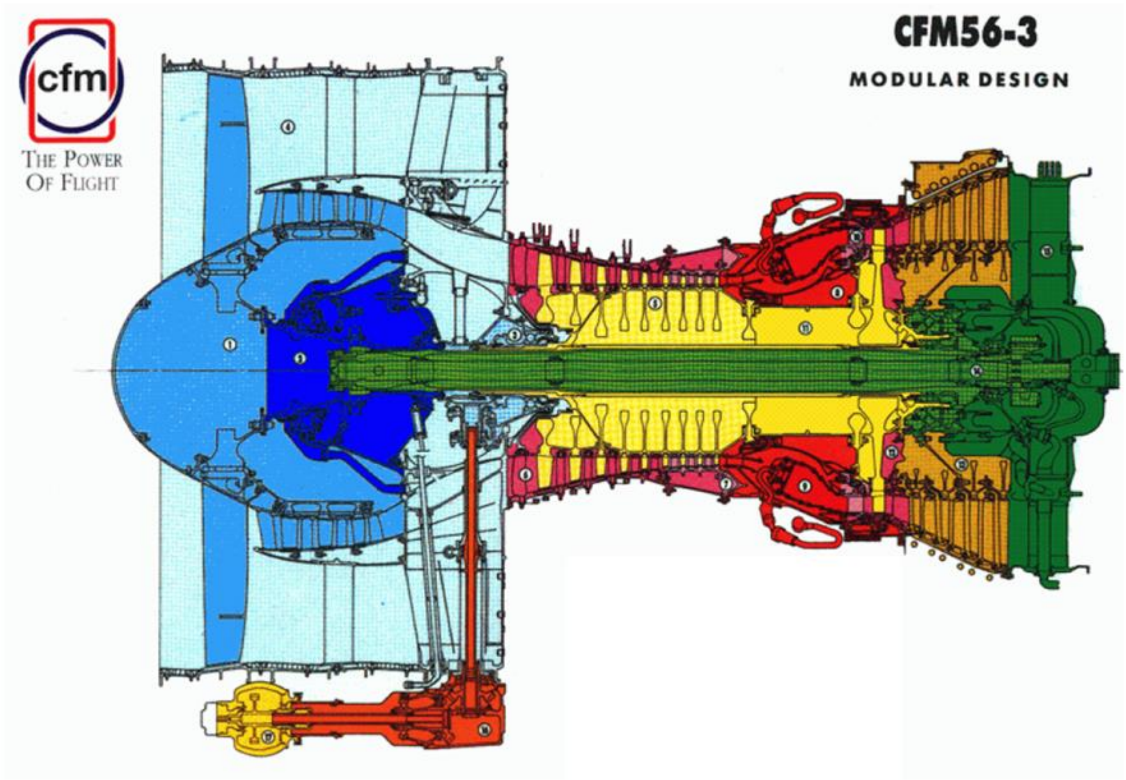

Figure 4.1: CFM56-3 schematic [50].

4.1 The Combustion Chamber

The combustor features a single-annular combustion chamber (see Fig. 4.2), contained in an inner and outer casing. It is a continuous ring, where the fuel is injected into the airflow and ignited, triggering the combustion chemical reaction, which raises the temperature and pressure of the flow.

The main component of this structure is the dome and it is where 20 circular holes are placed. In each of them, several components are located, such as a venturi, swirl nozzles and the fuel injectors. The venturi is composed by the secondary swirl nozzle and a convergent/divergent inlet, which has the purpose of accelerating the air-fuel mixture from the primary swirl nozzle already rotating. The secondary swirl nozzle geometry induces a swirling air flow in the opposite direction of the air-fuel mixture. This configuration generates high turbulence in the flow, allowing the complete vaporization (atomization) of the fuel. Besides, due to the high velocity of the flow from the secondary swirl nozzle, the air generates a lower pressure zone next to the fuel injector. This zone is named the primary combustion zone and it is the hottest point in the reactor. Due to the referred lower pressure provoked by the swirl, a reversal flow is induced that entrains and recirculates a portion of the combustion gases. This contributes to the flame stabilization, provides continuous ignition and increases the time the droplets are inside the chamber, improving the combustion efficiency.

In spite of optimal air-fuel ratio (stoichiometric) be better in terms of energy transfer, for the materials of the combustion chamber and blades of the HPT (high pressure turbine), it can be impossible to support. In order protect the interior walls of the chamber, a process named film cooling is used. The process consists in introducing relatively cool air through small holes placed in the step between two adjacent panels and allows the surface to be covered by a thin air layer that removes the heat absorbed by radiation and protects the walls from the hot gases (see Fig. 4.3). To cool the flow before it reaches the nozzle of the high pressure turbines, air is also introduced in a posterior zone of the chamber, named secondary zone or dilution zone. This air is injected in air jets called dilution holes and reduces the temperature of the combustion products so that a temperature to maintain the integrity of the turbine blades, is achieved.

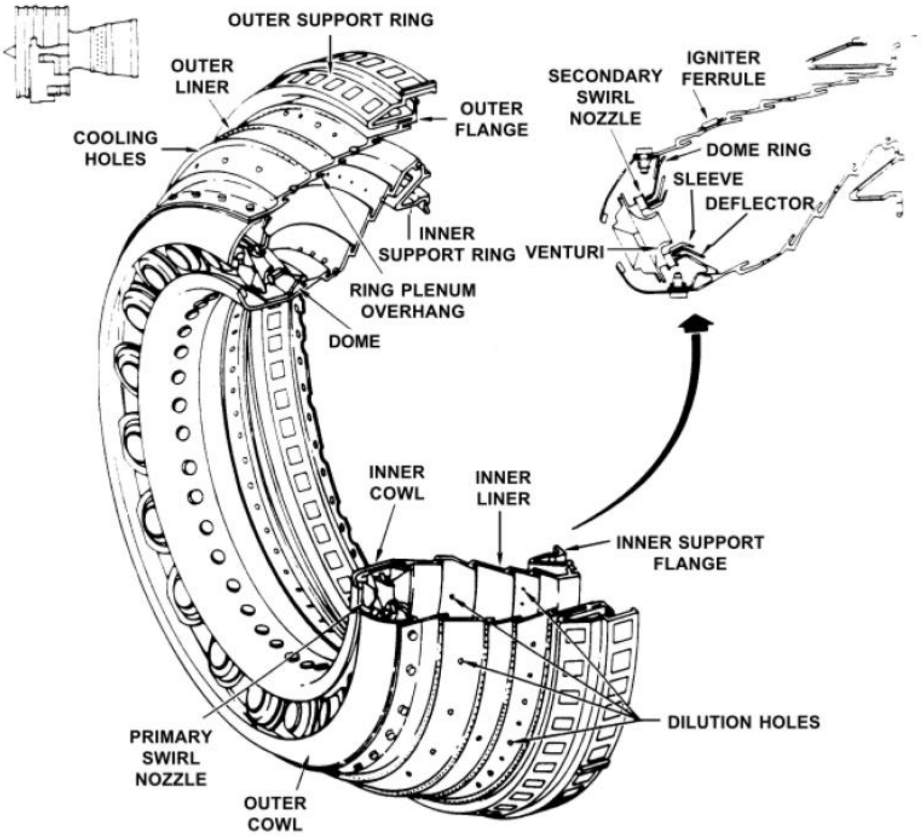

Figure 4.2: Combustion Chamber [50].

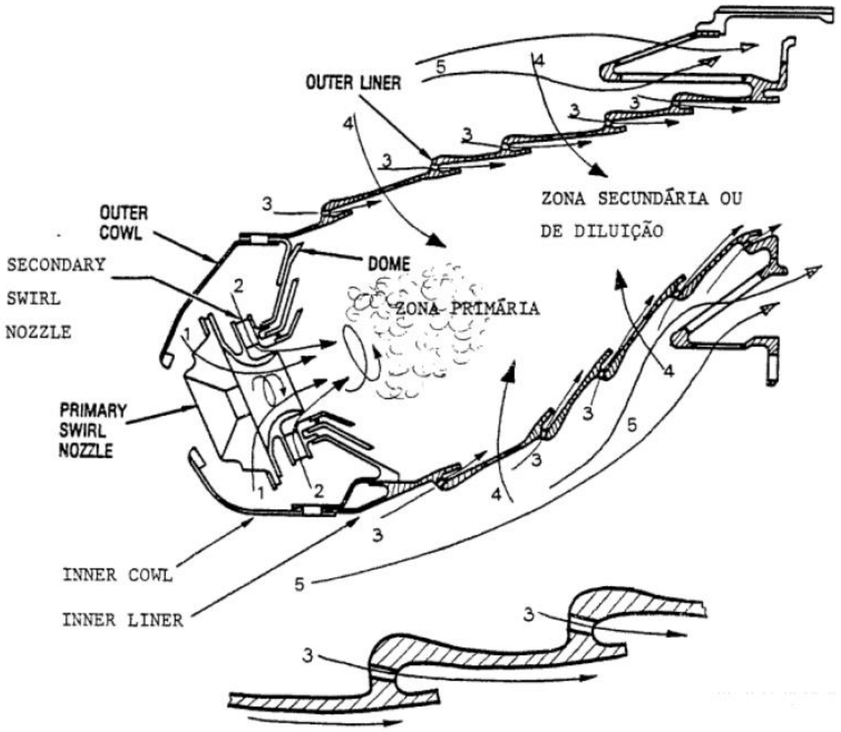

Figure 4.3: Flows in the Combustion Chamber. 1 – Primary swirl air flow; 2 – Secondary swirl air flow; 3- Film cooling air flows; 4 – Dilution air flows; 5 – Combustion Chamber bypass air flow for cooling the high pressure turbine [50].

4.2 Fuel Injection

The fuel injection is the final stage of the fuel delivery system. In CFM56, the fuel from the aircraft fuel supply system enters the engine at the fuel pump. Here, it is pressurized by the low pressure stage and flows through the main oil/fuel heat exchanger and fuel filter. Then, the fuel flows through the high pressure stage of the pump, the wash filter and gets into the main engine control. Here, the fuel is divided into metered flow and bypass flow, once the fuel pump has a higher fuel flow capacity than control system requires, porting back a portion to the outlet of the fuel pump low pressure stage. Finally, the metered fuel flows through the pressurizing valve, the flowmeter, the fuel manifold, and fuel nozzles into the combustion chamber [51]. While in other cases, engines use vaporizers as method to supply the fuel to the airstream, the CFM56-3 uses fuel spray nozzles.

4.2.1 Fuel Spray Nozzle

The purpose of the 20 fuel nozzles installed into the combustion case assembly and connected to the fuel manifold assembly is to deliver fuel into the combustor in a spray pattern, in order to provide a good light-off and efficient burning. Each of them has a primary and a secondary flow path, a flow divider, a check valve, fuel strainers and a dual orifice spray tip (see Fig. 4.4, Fig 4.5 and Fig. 4.6). The flow divider closes the secondary flow path during engine starting and low power conditions in order to assure the development of system pressures high enough to produce an adequate spray pattern even at low fuel flows [51].

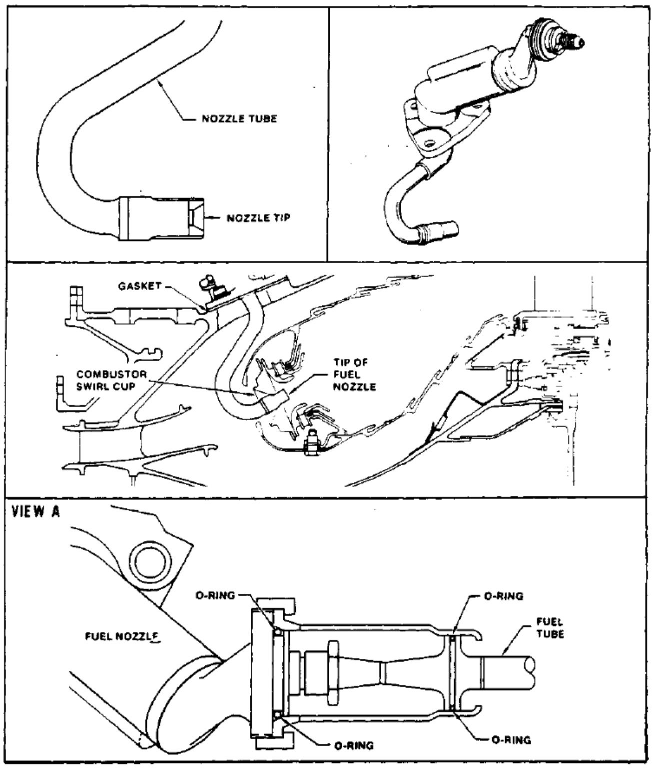

Figure 4.4: Fuel Nozzle installation [51].

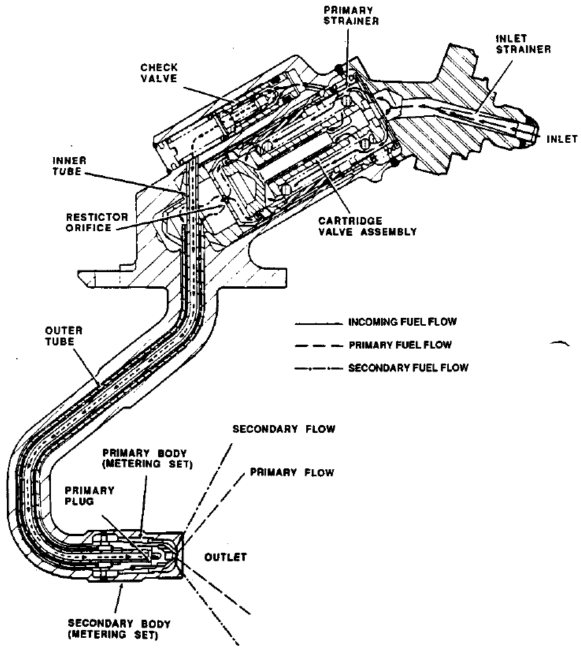

Figure 4.5: Fuel Nozzle cross section [51].

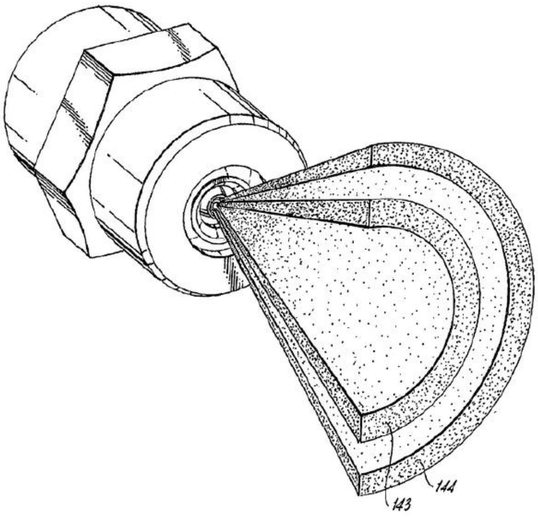

Figure 4.6: Dual orifice spray tip. 143 - primary and secondary spray; 144 - secondary spray [52]

4.3 Ignition System

The ignition system is essential to ignite the fuel-air mixture in the combustion chamber, not only in the starting cycle, but also continuously during take-off, landing and operation in adverse weather conditions. On those conditions, the reaction needs to be accelerated by an external source. Otherwise, the fuel and oxidiser would combine at a slow rate. Once in stable conditions, the reaction itself propagates, since the flame becomes an ignition source [51].

The ignition system can be divided in three main components: the two ignition exciters, which are capacitor discharge type exciters and provide starting and continuous duty ignition on demand; the two ignition Leads, with the purpose of transmitting high energy power from exciters and the two spark igniters.

4.3.1 Spark Igniters

The two spark igniters, or spark plugs, are located at the 4 and 8 o’clock position of the combustion case. When a $15KV-20KV$ or $14-18KV$ (on demand) discharge is transmitted to the electrode of the igniter plug, a potential is built up between the center electrode and the shell end ground electrode. The stored discharge current instantly arcs across the gap, emitting a high energy spark, responsible to ignite the fuel/air mixture in the combustor, as soon as this potential is sufficiently enough to ionize the annular recessed surface gap [51].

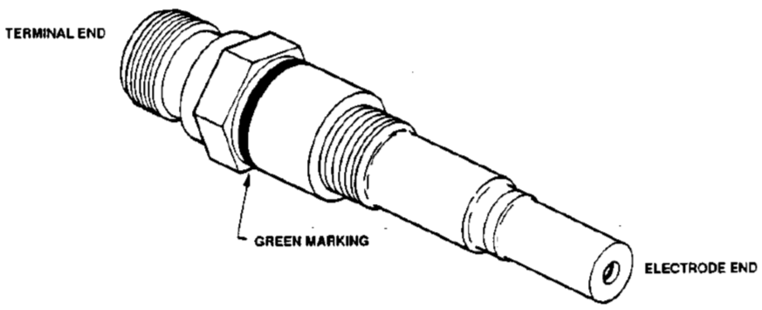

Figure 4.7: Spark Plug [51].

Chapter 5

Problem Modeling

CONVERGE was the software used to run the numerical simulation and was installed in a multi-Core igh performance computer. Before running, the simulation was pre-processed in CONVERGE Studio, the graphical user interface that accompanies CONVERGE and where all input files and data files related to the surface preparation and case setup were created. Output files were then post-processed again in CONVERGE Studio and EnSigh (see Fig. 5.1). This chapter includes a description of how the problem was modeled using the mentioned software.

CONVERGE is a computational fluid dynamics (CFD) program developed by Convergent Science. This company was created in 1997 by a group of graduate students from the University of Wisconsin-Madison, who designed meshes for KIVA[5], as a services organization and then they decided to develop their own CFD code, what became CONVERGE. The code was designed with the advice and guidance of a commercial engine manufacturer so it is designed specifically to address the key things that engines manufacturers, combustion designers and atomizer designers need. In 2008, Convergent Science sell the first CONVERGE licenses, with still only five employees. Since then, new offices were open in Detroit, New Braunfels and Linz, Austria and new distributors were signed in India, China, Korea and Japan. In 2014, the company held their first CONVERGE user conference and two years later a combustion summit in Nice, France. Currently they have about 100 employees. While a lot of their work is done to support internal combustion engines or piston engine designs, where they have about 90 of the 98 manufacturers in the world using the software, CONVERGE is also being used for gas turbines, pumps and compressors, exhaust aftertreatment, biomedical engineering, as well as other areas[53].

CONVERGE eliminates the grid generation from the simulation process. Unlike other CFD programs, it automatically generates an orthogonal, structured grid at runtime based on simple, user-defined grid control parameters. Usually, boundary-fitted grids morph the vertices and cells in the interior of the domain to conform to the shape of the geometry. This eliminates the benefits of numerical accuracy and computational efficiency when fitting a grid to a complex geometry, once it prevents the use of simple orthogonal grids. CONVERGE uses an innovative boundary-fitted approach that eliminates the need for the computational

---

[5] KIVA is a family of Fortran-based Computational Fluid Dynamics software developed by Los Alamos National Laboratory

grid to coincide with the geometry of interest. The grid used is chosen for computational efficiency instead of geometry. This allows the use of simple orthogonal grids, which simplifies the numerics of the solver. Besides, the grid generation complexity and the time required are greatly reduced, as the complex geometry only needs to be mapped onto the underlying orthogonal grid. CONVERGE uses surface triangles to cut the cells that are intersected by the surface at runtime. Generating the grid internally by the code at runtime allows the grid to be constantly changed, permitting scaling the cell size of the entire domain, locally refining or coarsening during the simulation, and adaptively refining the mesh[53].

Besides the grid generation, CONVERGE includes state-of-the-art numerical techniques and models for physical processing, including high fidelity spray models and an efficient detailed chemistry solver for combustion.

Before running a CONVERGE simulation, a set of ASCII-formatted input (**.in*) and data (**.dat*) files need to be prepared. While the input files contain numerical inputs, model parameters and boundary and initial conditions, data files contain thermodynamic properties, chemical reaction data, and surface geometry information. This input files are created and modified in the CONVERGE Studio graphical user interface. To begin with, the first step of the workflow was the surface preparation, where the geometry was imported through **.stl* files (can also be imported through a *surface.dat* file), the different boundaries were set by grouping triangles of the surface and the surface was cleaned. The second phase was the case setup, where the materials and physical models were selected, boundary conditions were defined, initial conditions and grid control were set and the output files pretended were chosen. The third step was running the simulation itself and finally, the output files were post-processed by line plotting 3D plotting. While the first, second and fourth phases are held in CONVERGE Studio[6], CONVERGE only runs the simulation itself.

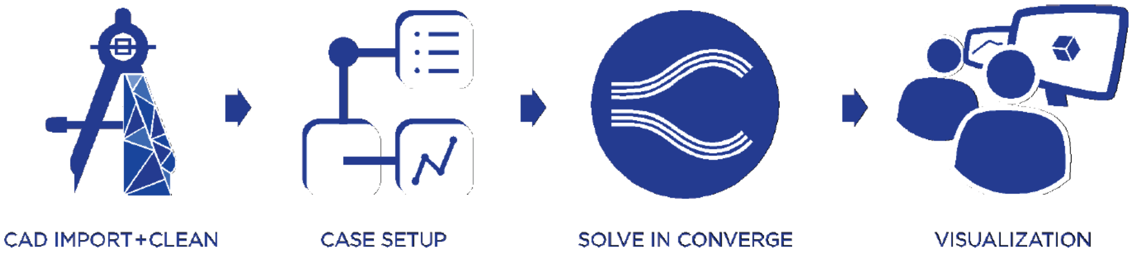

Figure 5.1: CONVERGE workflow.

5.1 Surface Preperation

---

[6] 3D plotting is only converted in CONVERGE Studio to a compatible EnSight format to be there analysed

5.1.1 Importing *.stl* files

The geometry used was ¼ of the engine constructed by Jonas[4], by performing a 3D scan on a real size combustor, gently provided by TAP, in which all the measurements were extracted to conduct a Computer Assisted Design with the commercial software CATIA V5. This geometry, divided in different *.stl* files for each component and boundary, was imported to CONVERGE Studio, which converted all the unit system from CAD units to CONVERGE units (meters). While importing, it was set a tolerance of 0,00001 meters for combining closely spaced vertices after conversion, as it was suggested by the software developer. When imported, CONVERGE Studio automatically divides the surface in triangles to define the geometry as an input file readable by CONVERGE. Due to the the surface being imported from separate *.stl* files and considering the tolerance set, a big amount of minute geometry defects arose between triangles of the different surface components (see Fig. 5.4).

5.1.2 Defining Boundaries

To easily manipulate the geometry and to set up boundary conditions and other features, the software allows to assign (“flag”) surface triangles into groups (“boundaries”). As the *.stl* files of each component of the the combustor were already in different files, CONVERGE automatically assigned the triangles of each component to a different boundary, as shown in Fig 5.2 and Fig. 5.3). Then, it was possible to hide and selected different boundaries to make it easier to see and repair surface defects, setup boundary conditions, specify grid refinement per boundary, define volumetric regions to set initial conditions, among other properties control.

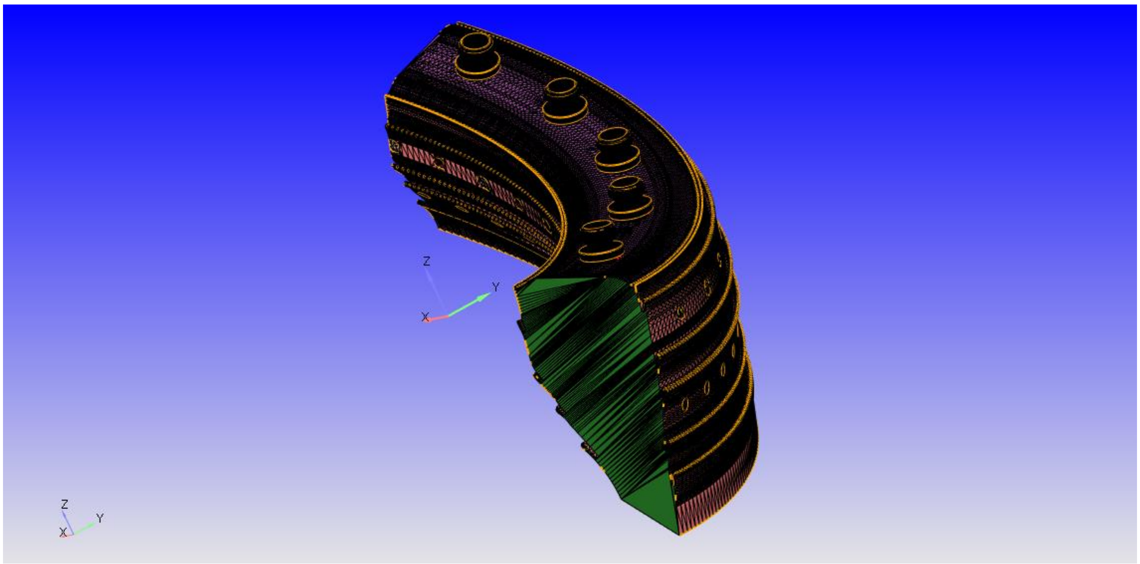

Figure 5.2: Triangles assigned to different boundaries distinguished by colors.

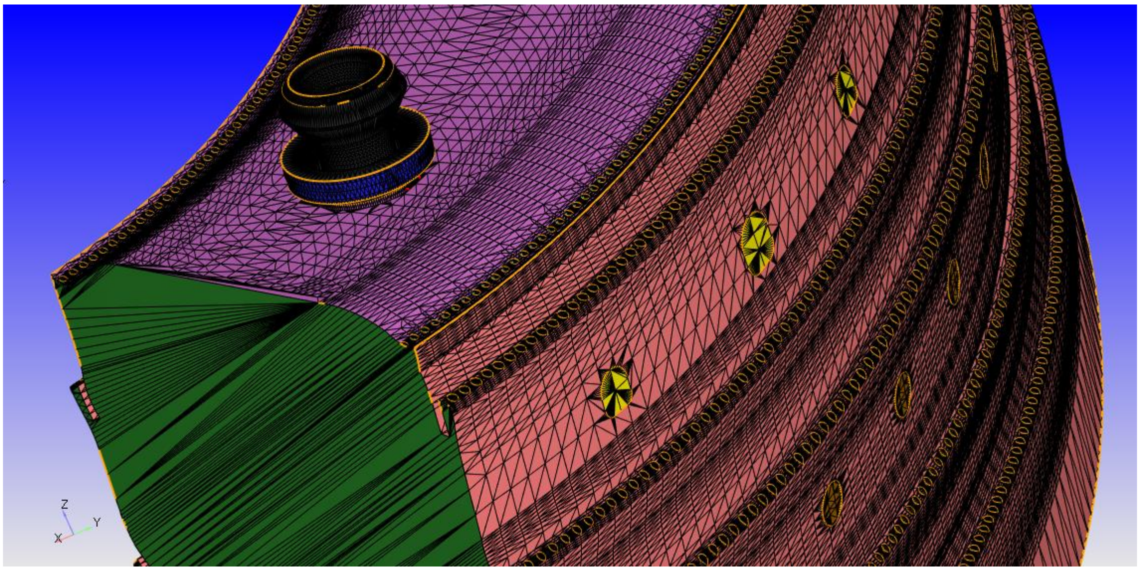

Figure 5.3: Detailed view of triangles assigned to different boundaries.

5.1.3 Geometry Defects

The software offers a *Diagnosis* dock, which can find all the defects in the geometry surface. While it is possible for CONVERGE to run with some of the defects, others prevents it to run, so it is important to find and repair them. Table 5.1 describes the critical defects found, after running this feature,:

Table 5.1: Type and number of defects found on the geometry surface.

Type of triangle defect	Number of defects
Intersections	53.172
Nonmanifold Problems	0
Open Edges	96.444
Normal Orientation	875
Isolated Triangles	0

In order to repair this defects, different techniques were applied with the help of the *Geometry* dock, such as delete, stitch, patch and by creating new triangles when needed. Most defects were found in the interface between different boundaries, where they came into conflict.

After having all defects repaired, the geometry was scaled to its original size, once the dimensions in the *.stl* files imported were in millimeters, and CONVERGE assumed them as meters.

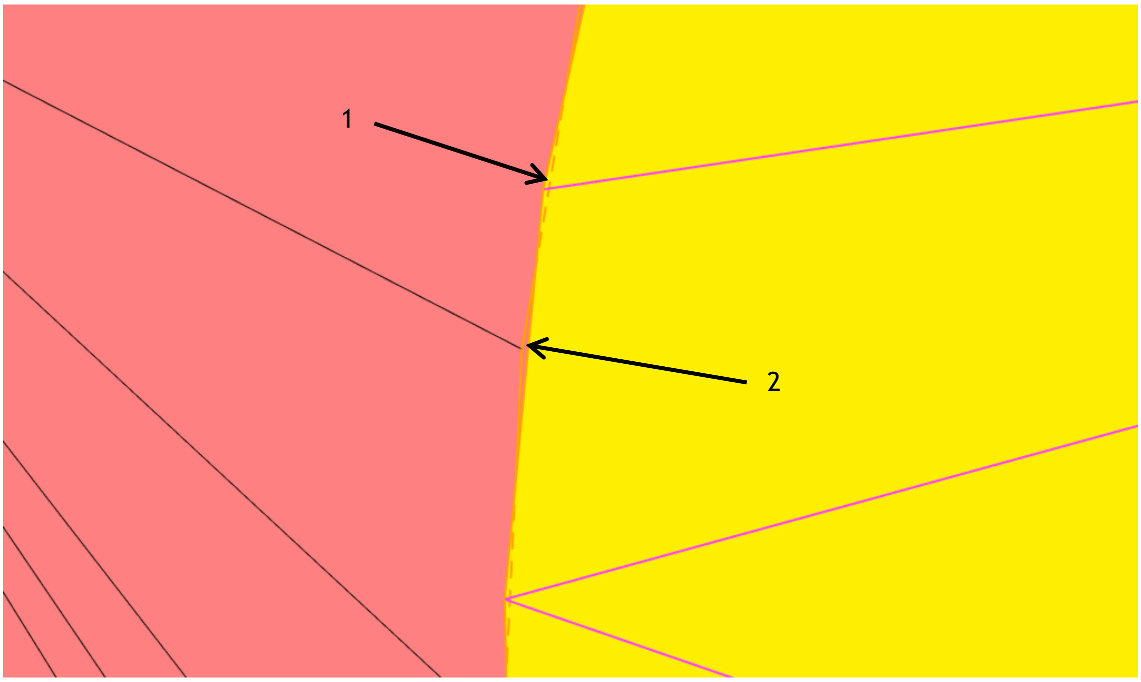

Figure 5.4: Example of defects arisen by conflict between two boundaries. 1 - Intersection; 2 - Open Edge

5.2 Case Setup

5.2.1 Materials

In order to define the type of simulation, “Gas simulation” and “Parcel Simulation” options were chosen, once we are are dealing with the injection of air and spray of liquid fuel. CONVERGE Studio software automatically enables the Global Transport Parameters for this options. Also, the “Reaction Mechanism” was set, so we could define the species to include in the simulation and the detailed chemistry for the combustion.

Regarding the gas simulation parameters, the Redlich-Kong equation of state was chosen, once it accounts for non-ideal gas behavior, which may be significant at high pressures and temperatures. The default critical temperature and critical pressure for the gas species in the simulation were set $133.0\ K$ and $3.77 \times 10^6\ Pa$, which are the appropriate values for air.

In order to process the simulation, all gas species involved in the combustion need to be specified, as well as all its thermodynamic data. A *therm.dat* file in the appropriate format was imported, containing all species and typical values. This file was a result from Wang, Ra, Jia and Reitz’s work[54] in the development of a reduced n-dodecane-polycyclic aromatic hydrocarbon (PAH) mechanism for modeling the combustion and soot formation processes of n-dodecane. This mechanism consists of 100 species and 432 reactions and was validated with available ignition delays and species concentration from shock tubes and jet stirred reactors.

As the injection of fuel was simulated through spray modeling of a liquid specie, a parcel simulation was used for the Jet-A. This liquid specie was imported along with its temperature-dependent properties.

Concerning the global transport parameters, the ratio of kinematic viscosity to thermal diffusivity (Prandtl number) and the ratio of kinematic viscosity to mass diffusivity (Schmidt number) were set, as suggested by the developer of the software, according to table 5.2:

Table 5.2: Global transport parameters.

Prandtl number	0.9
Schmidt number	0.78

Once we are simulating a combustion, values for each reaction between the species must be defined. A *mech.dat* file from Wang, Ra, Jia and Reitz's work[54] was imported with all reaction mechanisms for the gas species defined in the gas simulation.

5.2.2 Simulation Parameters

A transient solver was defined, resulting in a time-based full hydrodynamic simulation. The gas flow solver was set as compressible, whilst the liquid flow solver was set as incompressible. The simulation time parameters chosen are described in table 5.3:

Table 5.3: Simulation parameters

Start time	$0.0\ s$
End time	$0.1\ s$
Initial time-step	$5 \times 10^{-6}\ s$
Minimum time-step	$1 \times 10^{-7}\ s$
Maximum time-step	$0.00025\ s$

5.2.3 Boundary Conditions

A thorough definition of boundary conditions is fundamental for the success of a computational fluid dynamics simulation. All parameters for each boundary were configured with special attention. The main features of the boundary conditions, such as mass flow rates, temperature and pressure were based on Pedro's work[55], where he investigated the thermodynamic model of the CFM56-3 using GasTurb, a powerful cycle program used for simulating the most common types of GTE's, and Jonas's work[4], where he determined the percentage of primary zone and cooling air through an extensive trial and error approach. Four types of boundary were used: wall, inflow and outflow and symmetry.

Walls

Three geometry components were defined as walls: the swirl cones, the dome and the inner and outer liners. Velocity, temperature and roughness conditions were set to vary with Law-of-the-wall functions, with the following initial conditions: temperature of $744.0\,K$, as it is the air temperature calculated by Pedro that exits the HPC (see table A.1), which in part contours the liners of the combustor; absolute roughness of $0.0\,m$ and roughness constant of 0.0; Turbulent Kinetic Energy was set as zero normal gradient, once wall boundary type involves no transfer between the wall and the fluid and for the Turbulent Dissipation a Dirichlet turbulent dissipation was set.

Inflows

Values for mass flow rates were first obtained dividing by four the total $\dot{m}_a$ and $\dot{m}_f$ determined by Pedro in his work for the GTE operating at full power (see table A.1). Knowing the $\dot{m}_f$ and considering the air entering the Primary Zone at stoichiometric conditions ($AFR = 14{,}7$), Jonas determined the $\dot{m}_a$ entering the swirls. Then, the total cooling air was obtained just by subtracting the PZ $\dot{m}_a$ from the total $\dot{m}_a$. The percentage of cooling air for each boundary was also obtained by Jonas through an extensive trial and error approach through the simulations, in which the aim was to achieve the exit temperature reported by Pedro. The air mass flow input values are summarized in table 5.4. All inflow boundaries were set for air and considered composed only by oxygen (23%) and nitrogen (77%) also at a temperature of $744.0\,K$. Initial values for Turbulent Kinetic Energy and Turbulent Dissipation were also set but results were only analysed after converging for a value, once correct initial inputs were unlikely to be precisely calculated. k was set as a typical value of 0.01 and ε was set with values not greater than 10% of each boundary hole diameter.

Regarding fuel, instead of being simulated using an inflow boundary as Jonas did, a Spray Model was used and it is described further ahead in this work.

Table 5.4: Input values for air mass flow of each boundary, while burning Jet-A at full power.

Boundary	$\dot{m}\ (kg/s)$	**Coling air flow** $(\%)$
Swirler 1	1.7383	-

Swirler 2	1.7383	-
Dome holes	0.0127	0.1851
Dil 1.1	1.5000	21.9534
Dil 2	3.0000	43.9068
Dil 2.1	1.7000	24.8805
Mix	0.3000	4.3907
Mix 2	0.3000	4.3907
Mix 3.1	0.0050	0.0732
Mix 3.2	0.0050	0.0732
Mix 4	0.0100	0.1464
Total cooling air	6.8327	≈ 100
Total air	10.3092	
Fuel	0.2365	

Outflows

Only the exhaust of the combustor was defined as an outflow boundary and only its pressure was set according to Pedro's calculation ($2226.179\ kPa$). No velocity, temperature, species or backflow were defined, as it was pretended to be calculated by CONVERGE.

5.2.4 Regions and Initialization

In addition to the boundaries, a single region was defined to set initial conditions for the volume confined between all the combustor boundaries. Here also, an initial temperature, pressure and species were defined. However, the same parameters were only analysed after converging for specific values. The initial temperature was set as $744.0\ K$, pressure at $2343.346\ kPa$, determined by Pedro (see table A.1) to be the air pressure exiting the HPC, and three gas species: nitrogen, oxygen and Jet-A at stoichiometric conditions.

5.2.5 Physical Models

In this section, all inputs related to the physical models used in the simulation were set. Parameters for spray, combustion and turbulence modeling were defined for. It was exactly by changing the combustion modeling variables that the present work could study k-ε and k-ω models.

Spray Modeling

Spray modeling was used to configure nozzles, injectors and injection rate-shapes, set various spray-related constants, and define injection and drop models. The parcels were set to be distributed evenly throughout the cone, O'Rourke model was used to calculate the turbulent dissipation and the Frossling model to compute the drops evaporation. Values for the liquid fuel mass fraction, bin size and fuel vapor mass fraction for calculation of vapor penetration were set as 0.95, 0.001 and 0.001 respectively, typical values of for this type of simulation[53]. Mass diffusivity variables were not changed. NTC collision model was also set to better describe interactions between the parcels. Five injectors were set, each one with a nozzle, with precise location and direction inside the combustor. A solid cone spray was chosen with a 10 degrees cone angle, as shown is figure 5.5. For this last parameter, any information was found so the value was defined arbitrarily. The Kelvin-Helmholtz breakup model was used along with the Rayleigh-Taylor breakup model to simulate parcel breakup due to aerodynamic forces, as recommended by the software developers. Each injector were set to spray the fuel through parcels with a spray mass calculated by dividing by five the total $\dot{m}_f$ calculated in Pedro's work and multiplying it by the running time of the simulation 0.1 seconds. Nonetheless, the fraction of injected fuel was not set to be constant but to vary linearly from 0 to 1 in the first sixth, be constant for four sixths and from 1 to 0 in the last sixth of the running time, as outlined in figure 5.6.

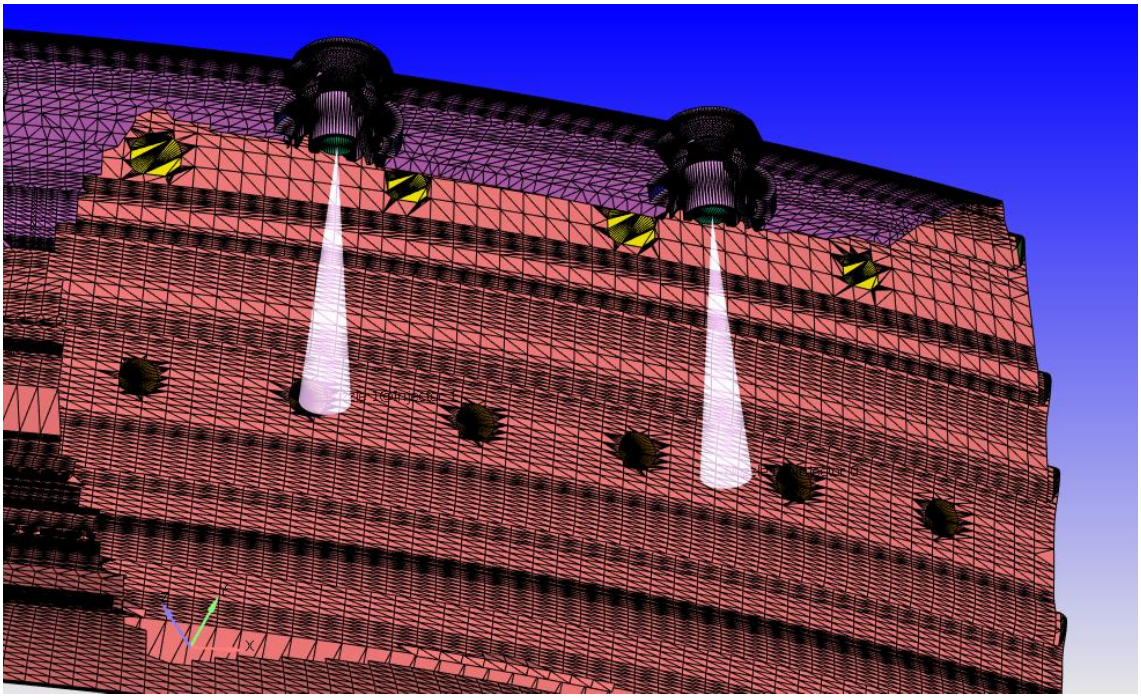

Figure 5.5: Injector with one nozzle spraying a solid 10 degree cone shape.

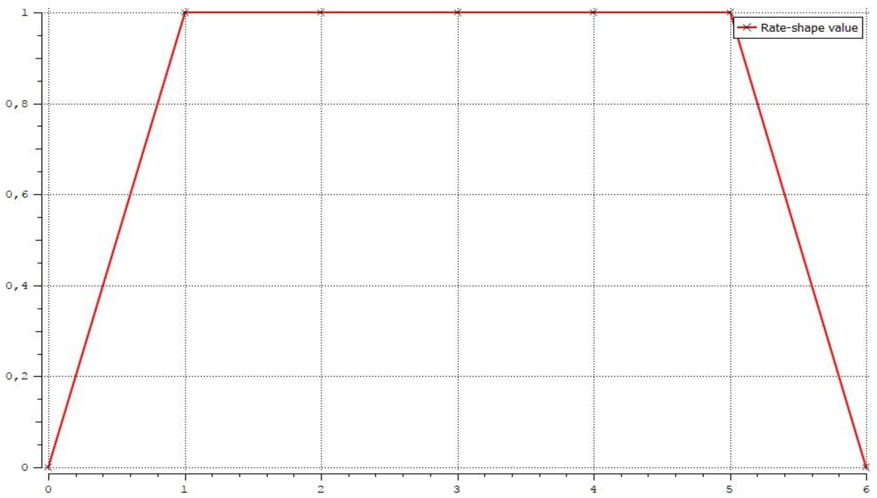

Figure 5.6: Spray rate of fuel throughout the simulation runtime in each injector.

Combustion Modeling

In this section the combustion model was set. SAGE detailed chemistry solver was chosen, once it is claimed by the developer to be the most predictive and accurate way to model combustion, ignition and laminar flame propagation inside combustion chambers. Start and end time for running the model were set the same as the whole running time of the simulation and the minimum cell temperature for SAGE activation was set to a typical value of $600.0\ K$ [53].

Turbulence Modeling

Comparing two different RANS models was the core of this work, being this section the one where parameters were changed between simulations. First, RANS option was chosen and then Standard k-ε or k-ω were set as the model for the numerical analysis. **Any model constant was ever changed**.

Source/sink Modeling

In order to be sure that the combustion started during the simulation an additional source of energy was added in the exact half of the runtime for a short instant of 0.01389 seconds, spherical form with a 5 millimeter radius and maximum temperature of $50000\ K$. This spark was later proved to be obsolete.

5.2.6 Grid Control

In the base grid options, it was defined the initial size of the mesh in the x, y and z directions. CONVERGE Studio is able to suggest a grid size based on a target cell count.

Considering the number of cells of Jonas's simulation (2.120.300) obtained with *HELYX-OS*, the software suggested a base grid interval of approximately $0.0013\,m$ in each direction. In order to guarantee similar initial base grid conditions, a value of $0.00125\,m$ was chosen for dx, dy and dz. Then the Adaptive Mesh Refinement was activated. A minimum cell count of 1 and maximum cell count of 2.500.000 were set, and velocity and temperature were selected to base AMR on their gradients.

5.2.7 Output/Post-Processing

In this last section, variables to be included in the output files, as well as the frequency for CONVERGE to write data files, were chosen and are presented in tables 5.5 and 5.6:

Table 5.5: Output variables selection.

Parameter	Variable
Typical Parameters	Density Mass Pressure Pressure gradients Temperature Velocity Vorticity
Combustion	Lambda Reaction ratio
Tubulence	Turbulence Dissipation Rate Ratio of turbulent and molecular viscosity Specific Turbulence Dissipation Rate Turbulent Kinetic Energy Turbulent length Scale Viscosity Dimensionless wall distance
Gas Species	Mass fraction (Jet-A) Mass fraction (O_2) Mass fraction (CO_2)
Parcel Species	Parcel Radius Parcel Temperature Parcel Velocity Parcel mass fraction (Jet-A)

Table 5.6: CONVERGE frequency of writing data files.

Time interval for writing 3D output data files	$0.001\ s$
Time interval for writing text output	$0.00005\ s$
Time interval for writing restart output	$0.002\ s$
Maximum number of restart files saved	3

Chapter 6

Results

Almost a year later of starting to get to know this revolutionary software, numerous case studies were made. As a recent developed software, any similar simulation case was found using CONVERGE neighter setup setings alike. The first challenge to overcome was to correct tens of thousands of minor surface defects that prevented the simulation to run. Also, it can not be counted, the number of simulations held, by varying input species and reaction mechanism data files, base grid conditions and even scale size of the combustor in order to achieve a combustion inside the chamber. Hence, the results presented should be interpreted considering always a margin of error, taking into account the hundreds of different parameters that this CFD analysis depends on. Nevertheless, acceptable conclusions can be made based on the results presented in this chapter.

In order to validate the results, a comparisation with Pedro and Jonas's works was made. However, there are big dirrences between the case setup from each study. For example, Jonas held a stationary pressure-based CFD analysis, while this work presents a transient, dependent of time simulation. Another main difference can be found on the fuel injection. While Jonas opted by reproducing the fuel injection through a wall inflow condition, this work used a set of models to simulate a parcel spray of fuel inside the combustion chamber. Despite this two major differentiations, the same input $\dot{m}$ values were used for fuel and each swirl and cooling air boundary. Considering the different and common features, the combustor exit $\dot{m}$, temperature and pressure are compared Pedro's results, and as well as a qualitative cross section temperature contour and turbulent kinetic energy contour is compared with Jonas's results.

As intended by this study, this chapter presents the results of two simulations set with the same parameters, except the turbulence model. Turbulence variables such as the Turbulent Kinematic Energy (k), Turbulence Dissipation Rate (ε), Specific Turbulence Dissipation Rate (ω), Turbulent Length Scale (l) and Friction Velocity (u^*) are compared between the models. Also y^+ values are shown at the combustor surface.

As a transient CDF analysis, results obtained were different throughout the runtime (see Fig. B.1). Considering that the injection-rate of fuel started and ended as zero, being contant for four sixths of the time, the result obtained can only be comared during a period when they are stable. Thus, and in order to compare results such as exit temperature, a mean result between only stable values was calculated, excluding initial and final time periods of the simulation.

All the values presented are a result of a CFD anlysis using a multi-core machine limited to 25 cores (number of licenses provided by Convergent Science to UBI) and 128 GB of RAM. While k-ε solution took about 9 hours, k-ω solution took near to 19 hours to simulate. In order to interpret the results, CONVERGE Studio post-processing tools were used. All graphics comparing both models were developed using CONVERGE Studio line plotting. All contour and 3D images were obtained through EnSight software after CONVERGE Studio convert the 3D output files to a readable format. Lastly, all the mean values were calculated by copying values from the output files (*.out*) to an Excell sheet and then using its calculation formulas.

6.1 Results Validation

Considering only a stable period between $0.03\,s$ and $0.08\,s$, a mean value for the exit $\dot{m}$, temperature and pressure was calculated. Regarding the mass-flow rate, the results show a mean value of $10.64\,kg/s$ with k-ε and $10.55\,kg/s$ with k-ω, about 0.79% and 0.81% difference than the value obtained by Pedro (see table A.1). As for the mean temperature, $2078{,}0\,K$ and $2053{,}1\,K$ represent a difference of 21% (k-ε) and 20% (k-ω). Lastly, the mean pressure was $2276{,}067\,kPa$ for k-ε and $2282{,}528\,kPa$ for k-ω, presenting a difference of 2.2% and 2.5%. While values for mass flow rate and pressure are naturally very close to the ones calculated by Pedro, the same did not happen with the temperature, which presented a bigger difference. The closest temperature was obtained with k-ω turbulence model, but only about 1% better accuracy. Figure 6.1 shows the average eaxhaust temperature during the simulations.

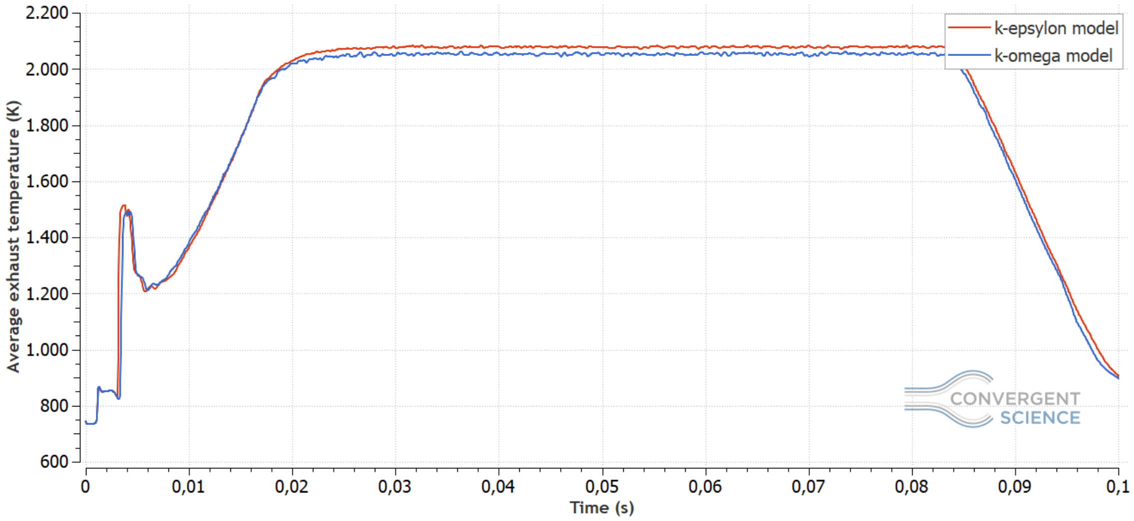

Figure 6.1: Average exhaust flow temperature.

A comparization with Jonas's work of a temperature and a turbulent kinetic energy contour was also made (see Fig. 6.2). As a transient CFD analysis, a particular instant for interpreting results needed to be chosen: exactly at half time of the simulation: $t = 0.05\,s$. Figures 6.2 and 6.3 show a cross section of this contours near the inlets. In the present work, it can be observed an higher temperature somewhat closer to the inlet, but also an overall higher temperature in the rest of section. In addition, it can be noticed that cooling duilution holes in the inner liner were not efficiently injecting air, which can lead to the higher exhaust flow temperature mentioned above. About k, a complete different result is found in this study and could be explained by the entirely distinct inflow setups regarding the fuel injection. It can be noticed that the higher values of Turbulent Kinetic Energy occur closer to center of the combustor, instead of near the inlets.

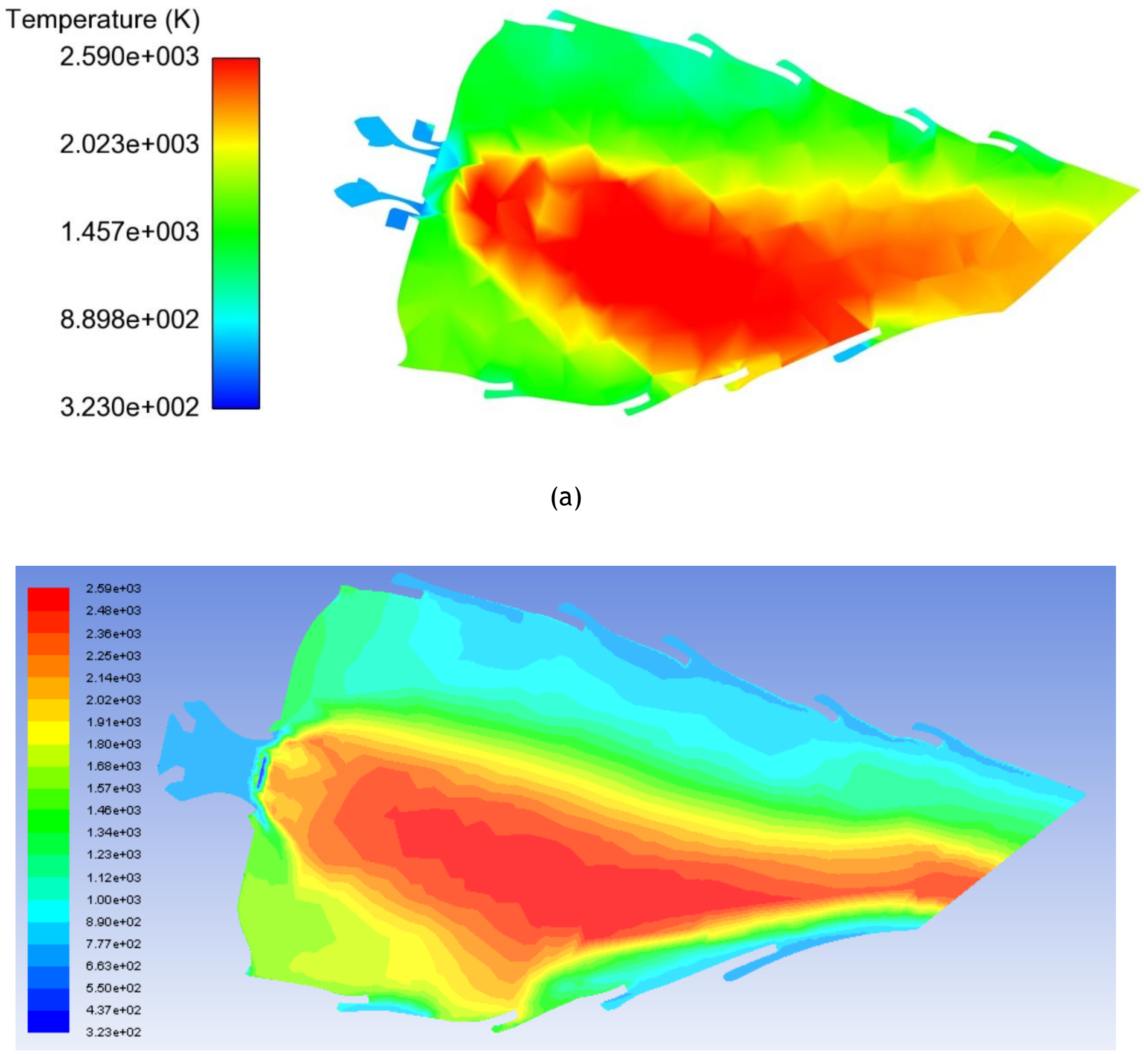

(a)

(b)

Figure 6.2: Temperature contours: (a) present study, and (b) Jonas's study[4].

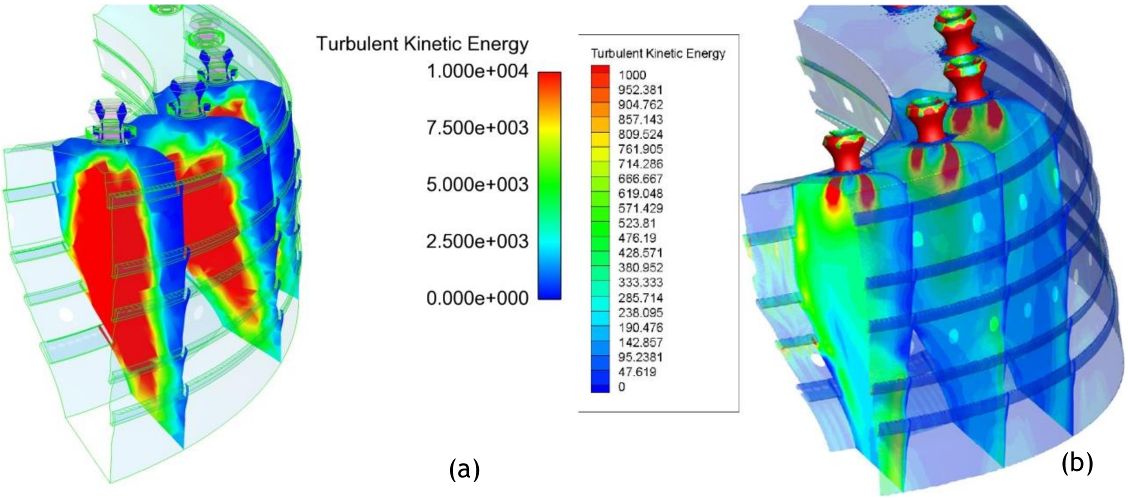

Figure 6.3: Turbulent Kinetic Energy contours: (a) present study, and (b) Jonas's study[4].

6.2 Turbulence Models Analysis

As a complicated flow with sudden changes in the main stream rate and a very complex surface, the results are not expected to be quantitatively good. However, a qualitative analysis may be done. In order to compare the models, several turbulence parameters are presented. All parameters analysed seem to behave similarly along the runtime with both models. However, and despite of all being found in the same order of magnitude, the absolute values show a considerable difference between them. As presented in the figure 6.4, the Turbulent Kinetic Energy, during stable period, gives an average value of $4554.23\ m^2/s^2$ for k-ε and $1421.90\ m^2/s^2$ for k-ω. Regarding The Turbulent Dissipation Rate, an average value of $2.12 \times 10^7\, m^2/s^3$ for k-ε and $0.54 \times 10^7\, m^2/s^3$ for k-ω was obtained (see Fig. 6.5). For the Specific Dissipation Rate of TKE, in turn, simulations have shown an average value of $43003.3\ 1/s$ for k-$\varepsilon$and $33312.5\ 1/s$ for k-ω (see Fig. 6.6). Lastly, in figure 6.7, we can find the Length Scale results, with an average value of about $0.00275\, m$ for k-ε and $0.00189\, m$ for k-ω. The difference between the results of each model regarding this four parameters can be explained as a result from the ε-equation overprediction of the turbulent length scale in the k-ε model, in the presence of adverse pressure gradients[47] and considering the correlations between this parameters given by the equation (2.33) and closure the coefficients (2.36). All this results are summarized in table B.1.

Regarding the dimensionless wall distance, values are expected to range between $30 < y^+ < 300$ once wall functions were used for both simulations. In figure 6.9 we can see the values obtained from k-ε and k-ω models. It can be observed that the ω-equation model results present more wall surface areas within this range than the ε-equation model, however, both still present some surface areas outside the range. The complexity of the walls surface shape, including for instance the dilution holes for wall cooling, may be the origin for CONVERGE to overestimate this parameter. An average value was not possible to calculate, once no output file with y^+ results could be copied to an Excell sheet as only 3D files were created by CONVERGE. Nevertheless, looking at the figure, the simulation with k-ω model may present an average value for y^+ closer to the upper limit. This results can be considered according to the friction velocity results (figure 6.8) though, which can be directly correlated through the equation (1.27).

Any of the models can be considered better than the other, but only different. This CFD analysis is very complex and depends on a set of models, which in turn, rely on constants that must not be considered ideal for every turbulent flow in the world. Thus the interpretation of the results should be to compare models and not to assume a more accurate one.

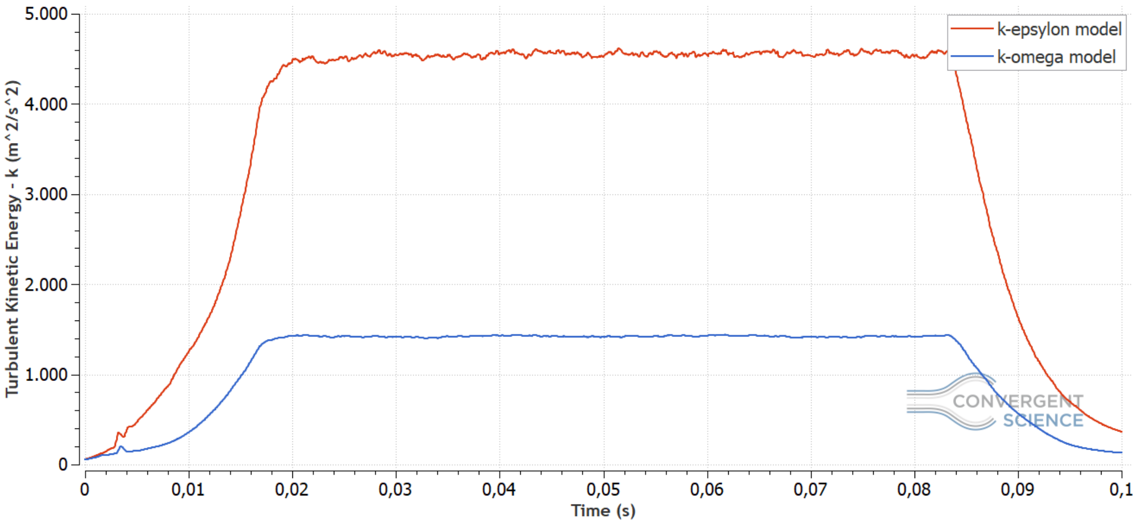

Figure 6.4: Turbulent Kinetic Energy (k) results from k-ε and k-ω models.

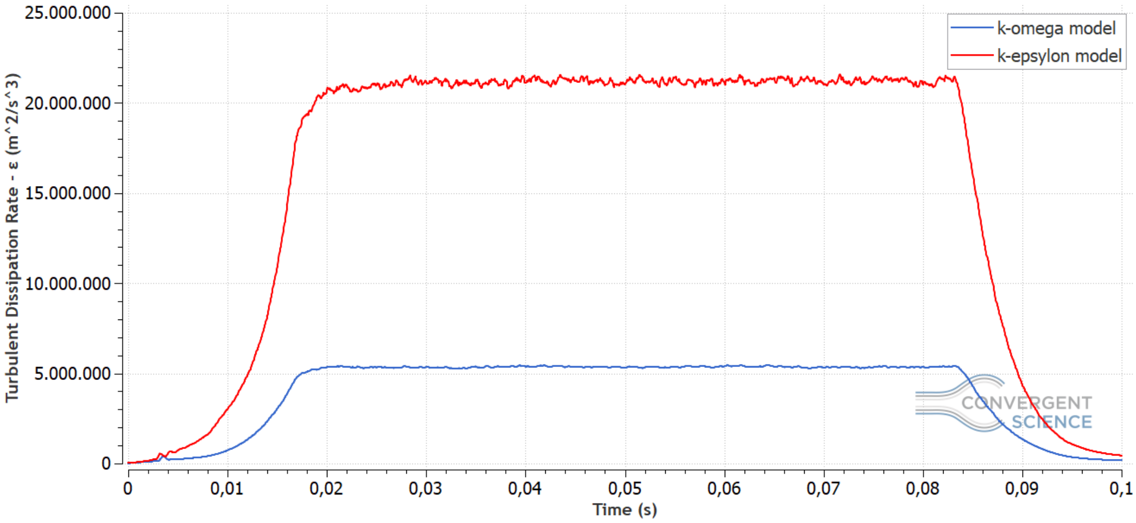

Figure 6.5: Turbulent Dissipation Rate (ε) results from k-ε and k-ω models.

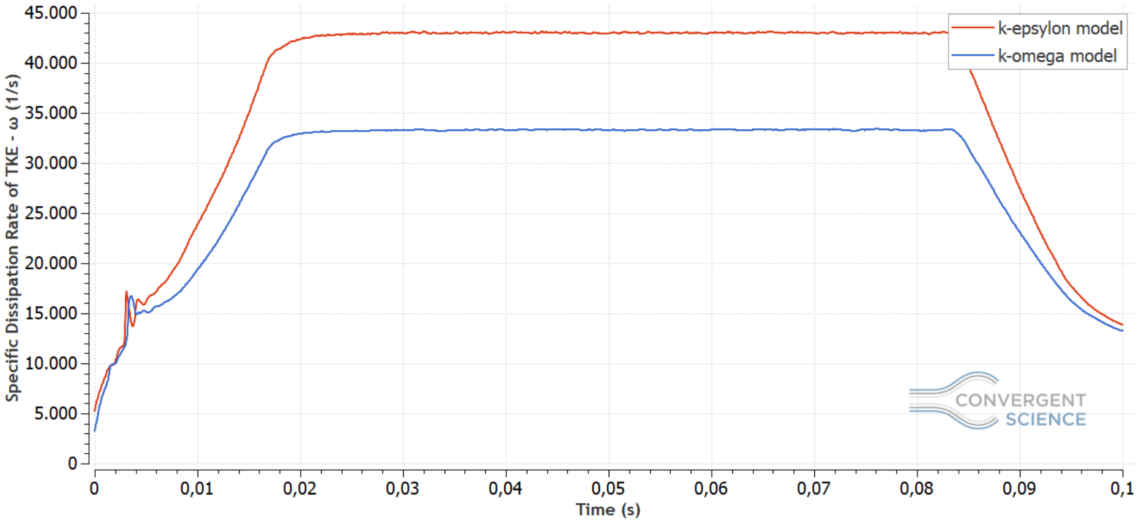

Figure 6.6: Specific Turbulent Dissipation Rate (ω) results from k-ε and k-ω models.

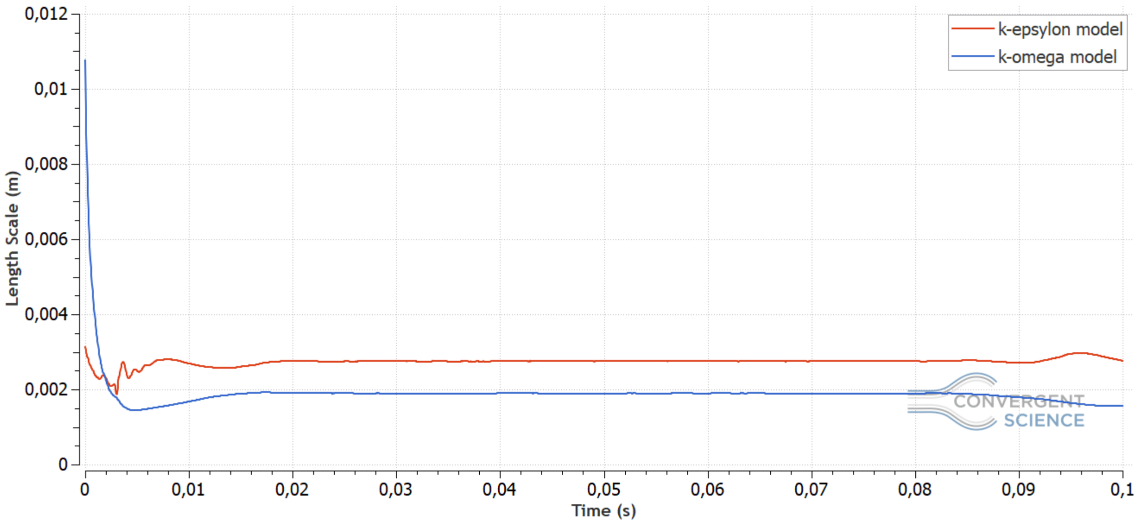

Figure 6.7: Length Scale (l) results from k-ε and k-ω models.

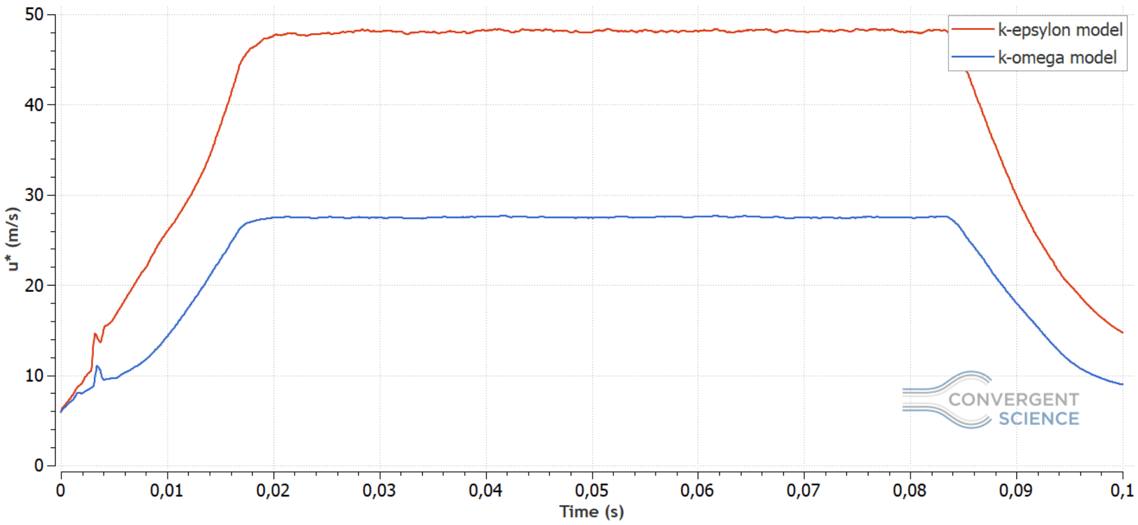

Figure 6.8: Friction Velocity near the walls (u^*) from k-ε and k-ω models.

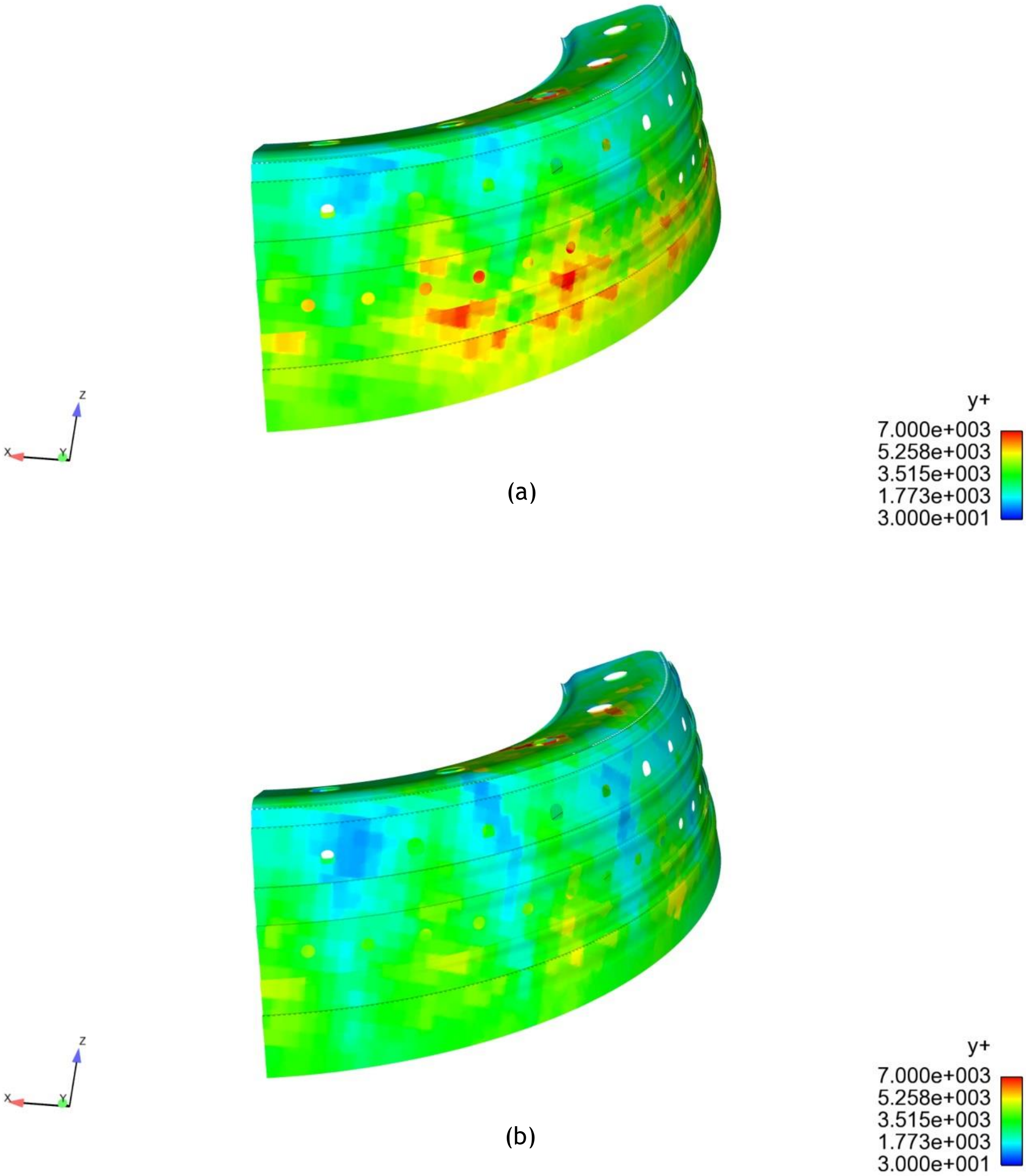

(a)

(b)

Figure 6.9: Dimensionless wall distance (y^+) results: (a) k-ε model, and (b) k-ω model.

6.3 Conclusion

This study consisted in a numerical analyses of the combustion of Jet-A in the annular combustor of the CFM56-3 engine, through two different turbulence models. The geometry used was ¼ of the engine constructed by Jonas Oliveira by performing a 3D scan on a real size combustor. This geometry was imported and prepared in a Computer Fluid Dynamics software, CONVERGE Studio, where the case setup was configured. The simulation was run on the main software CONVERGE installed on a multi-Core high performance machine installed in Universidade da Beira Interior. After the simulation, the results were visualized and post-processed in CONVERGE Studio. The final goal of this study was to compare the behavior of each turbulence model when studying the performance of an annular combustors similar to the most popular turbofan engine's. The turbulence models chosen were the standard k-ε and the standard k-ω and also a set of models were defined in order to simulate the injection of fuel through a parcel spray and, thus, better predict the flow inside the combustor.

When studying such a complex CFD problem, hundreds of different variables can affect the outputs and numerous setup parameters are needed to be defined. Just having a simulation solution itself, with the combustion happening and results within the order of magnitude expected, is already a great achievement. Thus, and as expected, several obstacles were ecountered, one after another, costing sometimes months to overcome. The software itself was a challenge. In spite of being more user friendly than most common CFD softwares and being capable to develop a mesh itself, any similar setups were found using CONVERGE. Besides, anyone in UBI had ever used the software, neither other portuguese users were known. The problem setup was a continuous learn-by-doing, failing and trying again process. By the time of the surface preparation, thousands of minute surface defects were found because of the tolerance while importing the *.stl* files. This defects prevented CONVERGE to run and were manually corrected, using several techniques from a geometry modification dock. After correcting the surface, it was necessary to scale the geometry for the appropriate measurments. Here, CONVERGE Studio presented a major drawback, once every time the geometry was scaled, it just disappeared from the graphical window. The reason behind this problem was not known but can be related to the graphic card limitations of the computer. The first solution found was to scale it gradually. Although, it was not enough and a second solution was used. In order to be able to setup all the simulation conditions, a sphere with 5 meters radius was created next to the geometry and its surface assigned to a boundary. With this, the combustor never disappeared again and it was only necessary to delete this sphere before exporting the input files. Then, countless were the simulations held that ended without ingniting the combustion. Several changes in the setup were made, since the introduction of a spark igniter, change the AFR to a richer mixture, manipulation of the mesh but it turned out to be the *therm.dat*, which was not specifying the reaction of a particular species present in the *gas.dat* file. After importing two compatible files with Jet-A thermodynamic data, finally the combustion happened and the results were extracted.

Regarding the results obtained from the CFD analysis, they can be considered acceptable after the validation made by comparing quantitatively the exhaust temperature, mass flow rate and pressure with Pedro's work, and qualitative comparization of a temperature and turbulent kinetic energy contour with Jonas's work. The major difference was found in the mean exhaust temperature (about 20%) and in the TKE. Although, they can be a result from the different setup conditions, as for example, the fuel injection through a parcel spray instead of a inflow wall boundary condition, or the fact that the present work is held with a transient solver in alternative to a steady-state.

When comparing the turbulence models, six main parameters were analysed: Turbulent Kinematic Energy (k); Turbulence Dissipation Rate (ε); Specific Turbulence Dissipation Rate (ω); Turbulent Length Scale (l); Friction Velocity (u^*); and the dimensionless wall distance (y^+). Both models demonstrated a similar behavior in all the parameters, along the runtime. The results were also all within the same order of magnitude, although the absolute values have shown a considerable difference. The ε-equation overprediction of the turbulent length scale in the k- ε model, in the presence of adverse pressure gradients could explain the differences regarding l, k, ε and ω parameters, while the complex surface geometry of the surface may be the reason behind the over prediction of y^+ and u^* values. Nonetheless, any turbulence model can be considered better than the other, once a CFD analysis like this is very complex and depends on a set of models and variables, which in turn, rely on constants that must not be considered ideal for every turbulent flow.

Overall, and after one year, working with CFD was a very exciting challenge that always kept the author interested in the process of learning and to go further in face of obstacles. A lot of dedication, commitement and resilence was necessary to carry this analysis. However, it was essential for the author to enjoy the work that was being developed throughout the year and all the learnings he took from it. As a final note, the biggest author's learning is that there is not a perfect CFD analysis, but a balance between the deepness of the study and the resources available.

6.4 Future Studies

Many important factors and variables in the present work were not considered once it would imply even more complexity in the study. Nonetheless, they could result in results much closer to the reality. This work can evolve in the future, among other examples, by:

- Compute more variants of the turbulence models, such as the RNG k-ε, the Realizable k-ε, or the k-ω SST not using law-of-the-wall functions and study their viability near such complex wall surfaces;
- Compute more computationaly expensive CFD analysis using Large Eddy Simulation (LES) and study the turbulent flow inside the combustor with much more detail and accuracy;

- Explore the use of different spray, collision, evaporation and dispersion models, as well as nozzle parameters such as solid or hollow cones, cone angle, circular injection radius, among other features related to fuel injection;
- Explore the use of different combustion models and their influence on combustion efficiency and emissions;
- Assign thickness to the wall boundaries and study the heat transfer on solid species;
- Study a model optimization of the combustor design, using the Genetic Algorithm in CONVERGE.

Like those, much other examples could be given and any of them would lead to numerous other factors that could be studied.

Bibliography

[1] C. Chant, *A Century of Triumph: The History of Aviation*. New York, 2002.

[2] World Energy Council, “World Energy Resources | 2016,” London, 2016.

[3] A. Kharina and D. Rutherford, “Fuel efficiency trends for new commercial jet aircraft: 1960 to 2014,” *Int. Counc. Clean Transp.*, no. August, 2015.

[4] J. Oliveira, “CFD Analysis of the Combustion of Bio-Derived Fuels in the CFM56-3 Combustor,” p. 126, 2016.

[5] I. B. Celik, “Introductory turbulence modeling,” *West. Virginia Univ. Cl. Notes*, no. December, p. 94, 1999.

[6] J. Boussinesq, *Essai sur la Théorie des Eaux Courantes*. Paris: Imprimerie National, 1877.

[7] O. Reynolds, “On the dynamical theory of incompressible viscous fluid and the determination of the criterion,” *Philosophical Transactions of the Royal Society of London*, vol. 186, no. A. pp. 123–164, 1895.

[8] J. A. D. Ackroyd, B. P. Axcell, and A. I. Ruban, *Early Developments of Modern Aerodynamics*. Michigan: Butterworth-Heinemann, 2001.

[9] L. Prandtl, “Report on Investigation of Developed Turbulence [Translation of the National Advisory Commitee for Aeronautics],” *NACA TM 1231*, pp. 1–7, 1949.

[10] K. Oswatitsch and K. ar. Wieyhardt, “Ludwig Prandtl and his Kaiser-Wilhelm-Institut,” *Annu. Rev. Fluid Mech*, pp. 1–26, 1987.

[11] K. Andrei Nikolaevich, *Selected Works of A. N. Kolmogorov*. 1991.

[12] J. Rotta, “Statistische Theorie niehthomogener Turbulenz,” *ZeithSchrift fur Phys.*, vol. 131, pp. 51–77, 1951.

[13] E. R. Van Driest, “On Turbulent Flow Near a Wall,” *J. Aeronaut. Sci.*, vol. 23, no. 11, pp. 1007–1011, 1956.

[14] T. Cebeci and A. M. O. Smith, *Analysis of turbulent boundary layers*. Academic Press, Incorporated, 1974.

[15] B. S. Baldwin and H. Lomax, “Thin Layer Approximation and Algebraic Model for Separated Turbulent Flows,” *AIAA 16th Aerosp. Sci. Meet.*, p. 9, 1978.

[16] P. Bradshaw and D. H. Ferriss, “Calculation of boundary-layer development using the turbulent energy equation,” *J. Fluid Mech.*, vol. 46, no. 1, p. 83, 1971.

[17] B. J. Daly and F. H. Harlow, “Transport Equations in Turbulence,” *Phys. Fluids*, vol. 13, no. 11, p. 2634, 1970.

[18] J. C. R. Hunt, “Mathematical Models of Turbulence,” *J. Fluid Mech.*, vol. 57, no. 4, p. 826, 1972.

[19] B. E. Launder and D. B. Spalding, “The numerical computation of turbulent flows,” *Comput. Methods Appl. Mech. Eng.*, vol. 3, no. 2, pp. 269–289, 1974.

[20] P. G. Saffman, “A Model for Inhomogeneous Turbulent Flow,” *Proc. R. Soc. A Math. Phys. Eng. Sci.*, vol. 317, no. 1530, pp. 417–433, 1970.

[21] C. D. Donaldson and H. Rosenbaum, “Calculation of the turbulent shear flows through closure of the Reynolds equations by invariant modeling,” *Aeronaut. Res. Assoc.*, vol. Report No., 1968.

[22] B. E. Launder, G. J. Reece, and W. Rodi, “Progress in the development of a Reynolds-stress turbulence closure,” *J. Fluid Mech.*, vol. 68, no. 3, p. 537, 1975.

[23] J. L. Lumley, O. Zeman, and J. Siess, “The influence of buoyancy on turbulent transport,” *J. Fluid Mech.*, vol. 84, no. 3, pp. 581–597, 1978.

[24] C. G. Speziale, “Modeling the pressure gradient–velocity correlation of turbulence,” *Phys. Fluids*, vol. 28, no. 1, p. 69, 1985.

[25] C. G. Speziale and S. Sarkar, “Second-order closure models for supersonic turbulent flows,” *AIAA Pap.*, vol. XLV, no. 4, pp. 721–733, 1987.

[26] W. C. Reynolds, “Fundamentals of turbulence for turbulence modelling and simulation,” *Lect. Notes von Karman Insitute*, pp. 1–66, 1987.

[27] P. Bradshaw and W. A. Woods, “An Introduction to Turbulence and its Measurement, A volume in Thermodynamics and Fluid Mechanics Series,” p. 238, 1971.

[28] H. Gustavsson, “Introduction to Turbulence,” 2006.

[29] H. Tennekes and J. L. Lumley, *A First Course in Turbulence*. Cambridge: MIT Press, 1972.

[30] F. R. Menter, J. Schütze, and M. Gritskevich, “Global vs. zonal approaches in hybrid RANS-LES turbulence modelling,” *Notes Numer. Fluid Mech. Multidiscip. Des.*, vol. 117, pp. 15–28, 2012.

[31] R. H. Nichols, “Turbulence models and their application to complex flows,” *Univ. Alabama Birmingham*, 2001.

[32] A. Bakker, “Modeling Turbulence in Stirred Vessels: A Review and Recent Developments,” p. 161, 2004.

[33] S. Kurien and M. A. Taylor, “Direct Numerical Simulations of Turbulence Data Generation and Statistical Analysis,” *Los Alamos Sci. Number*, vol. 29, no. 29, pp. 142–151, 2005.

[34] Y. Zhiyin, “Large-eddy simulation: Past, present and the future,” *Chinese J.*

Aeronaut., vol. 28, no. 1, pp. 11–24, 2015.

[35] J. Smagorinsky, "General Circulation Experiments with the Primitive Equations I. The Basic Experiment," *Mon. Weather Rev.*, vol. 91, no. 3, pp. 99–164, 1963.

[36] C. Fureby, "Large Eddy Simulation : A Useful Tool for Engineering Fluid Dynamics," no. December, 2012.

[37] S. J. Collie, M. Gerritsen, and P. Jackson, "A review of turbulence modelling for use in sail flow analysis," p. 53, 2001.

[38] C. Nguyen, "Turbulence Modeling," *Mit*, vol. 1, no. 8, pp. 1–6, 2005.

[39] T. Saad, "Turbulence Modeling For Beginners," *Univ. Tennessee Sp. Inst.*, 2011.

[40] H. K. Versteeg and W. Malalasekera, *An Introduction to Computational Fluid Dynamics: The Finite Volume Method*. Pearson Education Limited, 2007.

[41] L. Davidson, "An Introduction to Turbulence Models," no. November, 2003.

[42] B. Cushman-Roisin, "Chapter 8: Turbulence," in *Environmental Fluid Dynamics*, Hanover, New Hampshire, 2014.

[43] S. B. Pope, *Turbulent Flows*. 2000.

[44] F. Liu, "A Thorough Description Of How Wall Functions Are Implemented In OpenFOAM," pp. 1–30, 2016.

[45] Douglas L. Sondak, "Wall functions for the k-ε turbulence model in generalized nonorthogonal curvilinear coordinates," 1992.

[46] D. C. Wilcox, "Turbulence Modeling for CFD." DCW Industries, Incorporated, p. 460, 1994.

[47] M. Woelke, "Eddy Viscosity Turbulence Models employed by Computational Fluid Dynamic," *Trans. Inst. Aviat.*, vol. 4, no. 191, pp. 92–113, 2007.

[48] Stephen R. Turns McGraw-Hill, "An Introduction to Combustion: Concepts and Applications." McGraw-Hill, p. 565, 2000.

[49] A. Liñán and F. A. Williams, *Fundamental Aspects of Combustion*. Oxford University Press, 1993.

[50] J. Leite, "CFM56-3: basic engine." TAP Maintenance & Engineering, Lisboa, 1992.

[51] CFM International, "CFM56-3 Systems Training Manual." Cincinnati, Ohio, 1990.

[52] S. J. Myers, "Single circuit multiple spray cone pressure atomizers," 2013.

[53] K. J. Richards, P. K. Senecal, and E. Pomraning, "CONVERGE v2.3 Manual," Convergent Science, Inc., Madison, WI, 2017.

[54] H. Wang, Y. Ra, M. Jia, and R. D. Reitz, "Development of a reduced n-dodecane-PAH mechanism and its application for n-dodecane soot predictions," *Fuel*, vol. 136, no. x,

pp. 25–36, 2014.

[55] P. Ribeiro, “Análise de performance da Família de Motores de Avião CFM56.” Master’s thesis, Instituto Superior de Engenharia de Lisboa, Portugal, 2012.

Appendix

Setup Inputs

Table A.1: Relevant data form Pedro's work[55].

Combustor Station	$\dot{m}_{total}(kg/s)$	$\dot{m}_{1/4}(kg/s)$	**Temperature** (K)	**Pressure** (kPa)
Entry	41.51	10.36	743.91	2343.346
Exit	42.58	10.64	1649.94	2226.179

Outputs

Table A.2: Average results for different turbulence parameters.

Parameter	$k-\varepsilon$	$k-\omega$
Turbulent Kinetic Energy (k)	$4554.23\ m^2/s^2$	$1421.90\ m^2/s^2$
Dissipation Rate of TKE (ε)	$2.12 \times 10^7\ m^2/s^3$	$0.54 \times 10^7\ m^2/s^3$
Specific Dissipation Rate of TKE (ω)	$43003.3\ 1/s$	$33312.5\ 1/s$
Length Scale (m)	$0.00275\ m$	$0.00189\ m$
Friction Velocity (u^*)	$48.1\ m/s$	$27.5\ m/s$

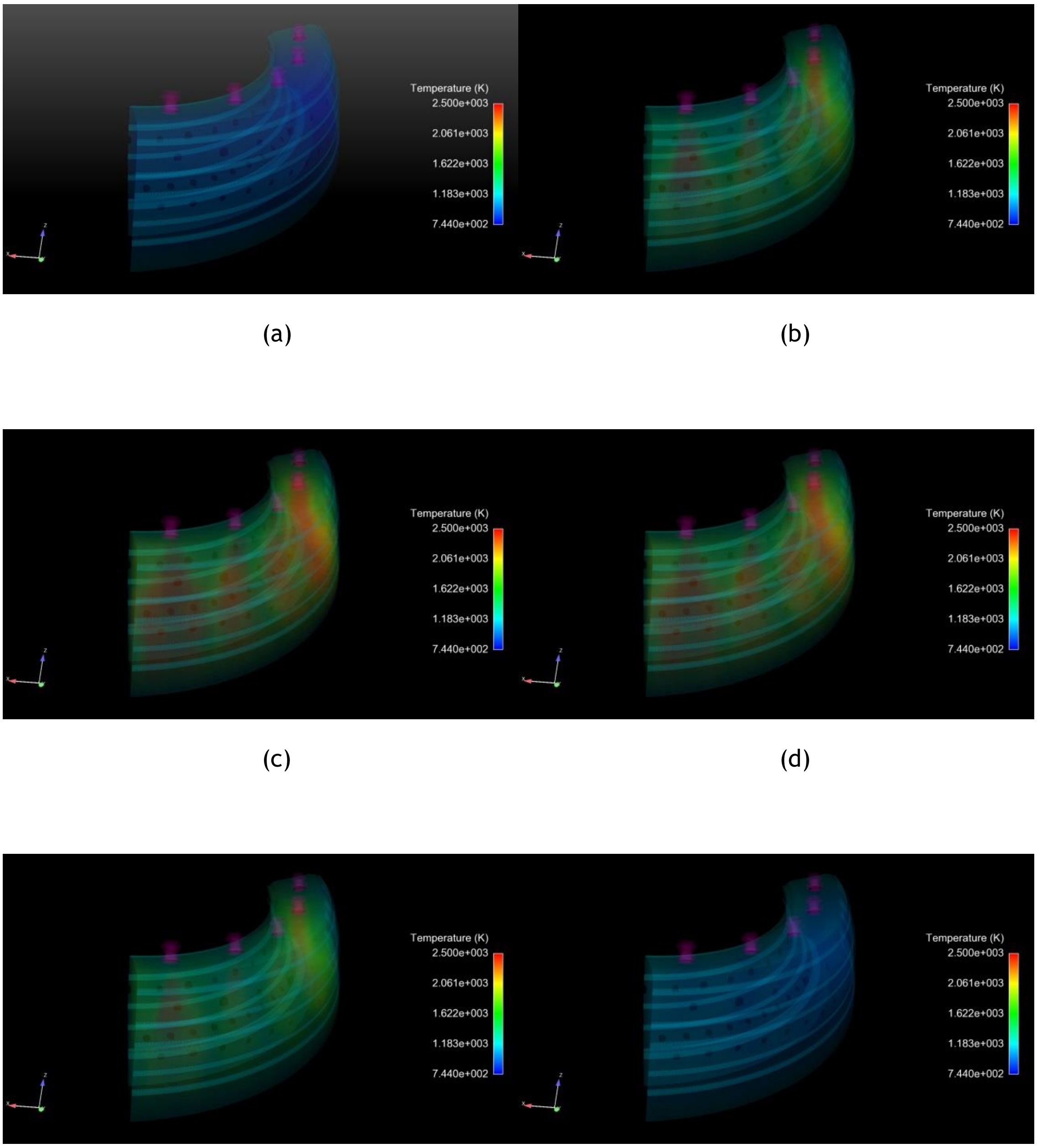

(a) (b)

(c) (d)

(e) (f)

Figure A.1: Temperature contours inside the combustion chamber: (a) $t = 0.000\ s$, (b) $t = 0.015\ s$, (c) $t = 0.050\ s$, (d) $t = 0.085\ s$, (e) $t = 0.090\ s$, and (f) $t = 0.010\ s$.